Monthly Notices
of the
ROYAL ASTRONOMICAL SOCIETY

MNRAS **497,** 5061–5075 (2020) doi:10.1093/mnras/staa2022

Factories of CO-dark gas: molecular clouds with limited star formation efficiencies by far-ultraviolet feedback

Mutsuko Inoguchi,[1★] Takashi Hosokawa,[2★] Shin Mineshige[1] and Jeong-Gyu Kim[3]

[1]*Department of Astronomy, Kyoto University, Sakyo-ku, Kyoto 606-8502, Japan*
[2]*Department of Physics, Kyoto University, Sakyo-ku, Kyoto 606-8502, Japan*
[3]*Department of Astrophysical Sciences, Princeton University, Princeton, NJ 08544, USA*

Accepted 2020 June 17. Received 2020 June 17; in original form 2020 April 1

ABSTRACT

The star formation in molecular clouds is inefficient. The ionizing extreme-ultraviolet radiation ($h\nu \geq 13.6$ eV) from young clusters has been considered as a primary feedback effect to limit the star formation efficiency (SFE). Here, we focus on the effects of stellar far-ultraviolet (FUV) radiation (6 eV $\leq h\nu \leq$ 13.6 eV) during the cloud disruption stage. The FUV radiation may further reduce the SFE via photoelectric heating, and it also affects the chemical states of the gas that is not converted to stars ('cloud remnants') via photodissociation of molecules. We have developed a one-dimensional semi-analytical model that follows the evolution of both the thermal and chemical structure of a photodissociation region (PDR) during the dynamical expansion of an H II region. We investigate how the FUV feedback limits the SFE, supposing that the star formation is quenched in the PDR where the temperature is above a threshold value (e.g. 100 K). Our model predicts that the FUV feedback contributes to reduce the SFEs for massive ($M_{\rm cl} \gtrsim 10^5$ M$_\odot$) clouds with low surface densities ($\Sigma_{\rm cl} \lesssim 100$ M$_\odot$ pc^{-2}). Moreover, we show that a large part of the H_2 molecular gas contained in the cloud remnants should be 'CO-dark' under the FUV feedback for a wide range of cloud properties. Therefore, the dispersed molecular clouds are potential factories of CO-dark gas, which returns into the cycle of the interstellar medium.

Key words: stars: formation – H II regions – photodissociation region (PDR).

1 INTRODUCTION

The evolution of galaxies is closely related to star formation activities. In nearby galaxies, the overall star formation rate is quite low; the cold molecular gas is converted to stars at a slow pace. The resulting depletion time-scale of the molecular gas is ∼Gyr over the galactic scale (e.g. Kennicutt & Evans 2012). In contrast, star formation occurs on a much shorter time-scale over small ($\lesssim$100 pc) cloud scales (e.g. Lee, Miville-Deschênes & Murray 2016). The lifetime of an individual giant molecular cloud (GMC) is estimated to be less than ∼10–30 Myr (e.g. Fukui & Kawamura 2010). A possible explanation for the above observations is that only a small fraction of the gas is used to form stars in each cloud. The physical processes responsible for such low star formation efficiency (SFE) are yet to be fully clarified.

A promising process to limit SFE is the so-called 'stellar feedback', which is radiative and kinetic energy injection from stars into natal clouds (e.g. Dale 2015; Naab & Ostriker 2017; Krumholz, McKee & Bland-Hawthorn 2019). The SFEs are lowered if the clouds are promptly destroyed by the feedback before a large part of the gas turns into stars. Recent studies show that such an evolution is indeed caused by the feedback from high-mass stars in GMCs (e.g. Kruijssen et al. 2019). It is further suggested that the cloud destruction advances over only a few Myr, which is shorter than the stellar lifetime. Therefore, radiation-driven or wind-driven bubbles expanding around high-mass stars before the first supernova explosion are believed to play an important role in GMC destruction.

H II regions created by the stellar ionizing (extreme ultraviolet, EUV; $h\nu \geq 13.6$ eV) radiation cause dynamical bubble expansion in GMCs (e.g. Yorke 1986). Because the expansion speed is supersonic with respect to the surrounding cold medium, the H II bubble expands, driving a preceding shock front. The shocked gas is taken into a shell around the H II region, which continues to expand, sweeping up the surrounding medium into the shell. While the gas dynamics varies depending on density structure of the clouds (e.g. Franco, Tenorio-Tagle & Bodenheimer 1990), theoretical studies have suggested that the resulting EUV feedback operates to limit the SFE (e.g. Whitworth 1979; Williams & McKee 1997; Matzner 2002; Kim, Kim & Ostriker 2016). In recent years, a number of authors have conducted radiation-hydrodynamics (RHD) numerical simulations that directly follow the EUV feedback in GMCs that are filled with turbulence in reality (e.g. Mellema et al. 2006; Dale, Ercolano & Bonnell 2012; Geen et al. 2015; Howard, Pudritz & Harris 2016; Gavagnin et al. 2017; Kim, Kim & Ostriker 2018; Haid et al. 2019; He, Ricotti & Geen 2019; González-Samaniego & Vazquez-Semadeni 2020). Overall, these studies have confirmed that the EUV feedback lowers the SFEs, though its impact depends on cloud properties, such as mass and surface density.

Extensive studies have been performed regarding ionizing radiation feedback. In fact, dissociating radiation (far ultraviolet, FUV; 6.0 $\leq h\nu \leq$ 13.6 eV) as well as ionizing radiation is emitted from young star clusters. Many studies have investigated the dynamical

★ E-mail: mutsuko@kusastro.kyoto-u.ac.jp (MI); hosokawa@tap.scphys.kyoto-u.ac.jp (TH)

effect of the radiation pressure of FUV radiation. Indeed, some of them show that the feedback caused by the radiation force contributes to regulate star formation in GMCs, although the resulting SFE is slightly higher than observations suggest (e.g. Raskutti, Ostriker & Skinner 2016, 2017; Thompson & Krumholz 2016; Kim et al. 2018).

Whereas the radiation pressure force is one dynamical aspect of FUV feedback, in this paper we consider the other aspect of thermal and chemical FUV feedback on GMCs. Hereafter, we use the terms EUV feedback and FUV feedback to designate the dynamical effects caused by H II regions and the thermal and chemical effects caused by photodissociation regions (PDRs), respectively. The FUV radiation creates a PDR, where the gas is heated up via a photoelectric effect, around an H II region (e.g. Hollenbach & Tielens 1999). The local Jeans mass is enhanced by such additional heating, which prevents the gravitational collapse of dense cores. As a result, the FUV radiation may further contribute to the reduction of SFEs in GMCs (e.g. Roger & Dewdney 1992; Diaz-Miller, Franco & Shore 1998; Inutsuka et al. 2015). For example, Forbes et al. (2016) show that photoelectric heating plays a dominant role in determining the star formation rate in dwarf galaxies (∼kpc-scale) rather than other feedback effects (but see also Hu et al. 2017). In the same vein, Peters et al. (2017) and Butler et al. (2017) have incorporated the FUV feedback in simulations following the star formation in a ∼ kpc-scale region of the Galactic disc, concluding that it is necessary to explain the observed depletion time-scale of ∼Gyr. On the individual GMC scale ($\lesssim$100 pc), by contrast, the effects of FUV feedback have not yet been fully investigated.

The low SFE means that most of the GMC gas is returned into the cycle of the interstellar medium, without being turned into stars. A part of such a 'remnant' gas may be recycled for the subsequent GMC formation. The stellar FUV radiation also substantially affects the physical and chemical states of the cloud remnants. As the FUV radiation destroys molecules via photodissociation, it generally creates cold H_2 gas associated with a small amount of CO molecules (e.g. van Dishoeck & Black 1988; Wolfire, Hollenbach & McKee 2010). Because such gas is difficult to observe via CO emission, it is called 'CO-dark' (van Dishoeck 1992). Recent observations via γ-ray (Grenier, Kaufman Bernadó & Romero 2005), dust continuum (Abergel et al. 2011) and C^+ line emission (Pineda et al. 2013; Pineda, Langer & Goldsmith 2014) suggest the existence of CO-dark gas, and no less than ∼30–70 per cent of the molecular gas is actually CO-dark in our Galaxy. Theoretical studies also support such Galactic-scale observations (e.g. Smith, Glover & Klessen 2014; Gong, Ostriker & Kim 2018). On the cloud scale, the appearance of CO-dark gas during the formation of molecular clouds has been suggested (e.g. Clark et al. 2012). However, the CO-dark gas phase while the clouds are being dispersed is yet to be further studied (e.g. Hosokawa & Inutsuka 2007; Gaches & Offner 2018; Seifried et al. 2020).

As seen above, the stellar FUV radiation should cause additional feedback that affects the SFEs and chemical compositions of the cloud remnants. Whereas fully considering such effects requires expensive numerical simulations of radiation magnetohydrodynamics, here we adopt a one-dimensional (1D) semi-analytical treatment that guides our understanding. Kim et al. (2016) have developed a semi-analytical model for the expansion of an H II region driven by photoionization and radiation pressure. The minimum SFEs limited by the EUV feedback have been evaluated as functions of the cloud masses and surface densities. However, they ignore the roles of FUV feedback. Hence, we construct a new model based on Kim et al. (2016), where both FUV and EUV feedback effects are included. In order to evaluate the FUV feedback, we solve the thermal and chemical structure of PDRs around H II regions assuming spherical symmetry. Although simple, this approach allows us to consider the effects of FUV feedback against a variety of GMCs that have different properties. We first investigate how much the FUV feedback contributes to reducing the SFEs. Next we consider the chemical compositions of the GMC remnants under the FUV feedback, showing that they are potential factories of CO-dark molecular gas.

Table 1. Parameter set.

$M_{\rm cl}$ ($M_\odot$)	$\Sigma_{\rm cl}$ ($M_\odot$ pc^{-2})	$R_{\rm cl}$ (pc)	n_0 (cm^{-3})
10^4	15–700	13.2–1.94	30–10 000
10^5	31–1506	31.9–4.60	30–10 000
10^6	67–3246	68.7–9.90	30–10 000

The rest of the paper is organized as follows. We present our models in Section 2, where we outline the overall methodology in Section 2.1. We describe how to couple the dynamics and the thermal and chemical processes operating in the PDRs in Sections 2.2 and 2.3, respectively. In Section 3, we show our main results. First, we present a representative case of the time evolution of the thermal and chemical structure in the PDR in Section 3.1. Then we study the effects of FUV feedback on limiting the SFE in Section 3.2, and possible chemical compositions of the cloud remnants in Section 3.3. We provide a relevant discussion and conclusion in Sections 4 and 5, respectively.

2 MODEL

2.1 Methodology

We first describe our model in this section. We consider spherical and uniform density clouds, which are characterized by the mass $M_{\rm cl}$ and surface density $\Sigma_{\rm cl}$. The cloud radius $R_{\rm cl}$ and hydrogen number density n_0 are related to $M_{\rm cl}$ and $\Sigma_{\rm cl}$ as

$$R_{\rm cl} = \sqrt{M_{\rm cl}/\pi\,\Sigma_{\rm cl}} \tag{1}$$

$$n_0 = \frac{M_{\rm cl}}{(4/3)\pi R_{\rm cl}^3 \mu_{\rm H}} = \frac{3\pi^{1/2}}{4\mu_{\rm H}} M_{\rm cl}^{-1/2}\Sigma_{\rm cl}^{3/2}, \tag{2}$$

where $\mu_{\rm H} = 1.4 m_{\rm H}$ is the mean molecular weight per hydrogen nucleus. We consider clouds with $M_{\rm cl} = 10^4$, 10^5 and 10^6 $M_\odot$. The surface density is varied so that the resulting number density should fall on a typical range of observed molecular clouds, $30 < n_0 < 10^4$ cm^{-3} (e.g. Tan et al. 2014). Table 1 summarizes the ranges of the parameter values we consider.

Our aim is to derive the minimum SFE required for cloud disruption $\varepsilon_{\rm min}$ as a function of the cloud mass $M_{\rm cl}$ and surface density $\Sigma_{\rm cl}$. We focus on the FUV feedback to limit the SFE. For a given set of ($M_{\rm cl}$, $\Sigma_{\rm cl}$), we start our calculation by putting a star cluster with the mass of $M_* = \varepsilon M_{\rm cl}$ at the origin. First, we take a trial value for the SFE ε. We envision that an H II region and surrounding PDR created by the stellar EUV and FUV radiation expands around the central cluster in the cloud. Following Kim et al. (2016), we calculate the EUV photon number luminosity as

$$S_{\rm EUV} = \Xi_{\rm EUV} M_*, \tag{3}$$

where the ratio of the stellar mass to the EUV luminosity $\Xi_{\rm EUV}$ is calculated with the SLUG code (Krumholz et al. 2015). Similarly, we

calculate the FUV photon number luminosity

$$S_{\rm FUV} = \Xi_{\rm FUV} M_*, \tag{4}$$

where we again use the SLUG code to evaluate $\Xi_{\rm FUV}$ (see the Appendix for details). We assume that Ξ is time-independent. This is a reasonable approximation, as the dynamical time-scale $t_{R_{\rm cl}}$ is shorter than the lifetimes of massive main-sequence stars. The dynamics of the expanding H II region and surrounding shell can be described by the analytical formula (see Section 2.2). The effects of the FUV radiation on the thermal and chemical structure outside the H II region are then calculated (Section 2.3).

These calculations are performed using the arbitrary choice of ε, and we determine the minimum SFE by the following iterative procedure. If ε first assumed is too small, only a small central part of the cloud is affected by the cluster radiation. Further star formation is possible for such a case, meaning that the minimum SFE should be higher. We repeat the calculations by increasing ε incrementally. If ε becomes sufficiently large, then the radiative feedback influences the whole natal cloud, leaving no room for further star formation. We assume that the minimum SFE $\varepsilon_{\rm min}$ is determined for such a case (Section 2.4). The obtained value of $\varepsilon_{\rm min}$ depends on the feedback effects considered. The FUV feedback potentially reduces the SFE in addition to the EUV feedback, because it heats the gas outside the H II region, hindering star formation. The above procedure is basically the same as in Kim et al. (2016), except that we additionally consider the stellar FUV radiation.

2.2 Dynamics of expanding H II regions

We model the dynamical expansion of an H II region created around the cluster in the natal molecular cloud. In what follows, we assume that the photoionized gas has the constant temperature $T_{\rm H\,II} = 10^4$ K for simplicity. The initial size of an H II region is determined by the so-called Strömgren radius

$$r_{\rm IF,0} = \left[\frac{3 S_{\rm EUV} f_{\rm ion}}{4\pi n_0^2 (1-\varepsilon)^2 \alpha_{\rm B}} \right]^{1/3}, \tag{5}$$

where $\alpha_{\rm B} = 2.59 \times 10^{-13} (T_{\rm H\,II}/10^4\ {\rm K})^{-0.7}\ {\rm cm^3\ s^{-1}}$ is the case B recombination coefficient (Osterbrock 1989), and $f_{\rm ion} = 0.73$ denotes the fraction of the EUV photons absorbed by the gas (not by the dust; Krumholz & Matzner 2009). We note that $f_{\rm ion}$ varies with the product $S_{\rm EUV} n_{\rm H\,II}$ (Draine 2011), although the thermal pressure force and the H II region size only weakly depend on $f_{\rm ion}$ as $r_{\rm IF} \propto f_{\rm ion}^{1/3}$ and $F_{\rm thm} \propto f_{\rm ion}^{1/2}$ (Kim et al. 2016).

Because the internal thermal pressure is much higher than that in the ambient medium, the H II region starts to expand. As considered in Kim et al. (2016), however, the dynamics of the H II region is generally affected by additional effects such as the radiation pressure exerted on the photoionized gas (e.g. Draine 2011) and swept-up shell (e.g. Krumholz & Matzner 2009; Ishiki & Okamoto 2017). However, we omit such additional effects for simplicity. Recent theoretical studies show that the radiation pressure effect is particularly important for disrupting GMCs with high surface densities $\Sigma_{\rm cl} \gtrsim 100\ {\rm M_\odot\ pc^{-2}}$ (e.g. Fall, Krumholz & Matzner 2010; Murray, Quataert & Thompson 2010). We separately examine its effects on our results in Section 4.3.

Once the H II region begins to expand, the ambient gas is swept up, to be retained in a shell. The shell is bounded by the ionization front and preceding shock front. The shell mass $M_{\rm sh}$ is estimated as

$$M_{\rm sh} = \frac{4}{3}\pi r_{\rm IF}^3 \rho_0 (1-\varepsilon) - M_{\rm H\,II}. \tag{6}$$

Here, $r_{\rm IF}$ is the radial position of the ionization front and $M_{\rm H\,II}$ is the mass of ionized gas,

$$M_{\rm H\,II} \approx \frac{4\pi}{3} r_{\rm IF}^3 \mu_{\rm H} n_{\rm H\,II}, \tag{7}$$

where the number density of ionized gas $n_{\rm H\,II}$ varies with ionization front radius as $n_{\rm H\,II} \propto r_{\rm IF}^{-3/2}$. The expansion law, or the time evolution of $r_{\rm IF}$, is derived with the equation of motion of the shell,

$$\frac{\rm d}{{\rm d}t}(M_{\rm sh} v_{\rm sh}) = F_{\rm out} - F_{\rm in}, \tag{8}$$

where $v_{\rm sh} = {\rm d}r_{\rm sh}/{\rm d}t$ is the shock velocity, and $F_{\rm out}$ and $F_{\rm in}$ represent the forces exerted on the outer and inner surfaces of the shell, respectively. As noted above, we only consider the thermal pressure of the ionized gas as the outward force $F_{\rm out}$,

$$F_{\rm thm} = 4\pi r_{\rm IF}^2\, 2 n_{\rm H\,II} k_{\rm B} T_{\rm H\,II}, \tag{9}$$

which scales as $F_{\rm thm} \propto n_{\rm H\,II} r_{\rm IF}^2 \propto r_{\rm IF}^{1/2}$. We ignore $F_{\rm in}$ for simplicity. Equation (8) is solved analytically, and we obtain

$$r_{\rm IF}(t) = r_{\rm IF,0} \left(1 + \frac{7}{4}\sqrt{\frac{4}{3}} \frac{c_{\rm s} t}{r_{\rm IF,0}} \right)^{4/7}, \tag{10}$$

where $c_{\rm s} = \sqrt{2 k_{\rm B} T_{\rm H\,II}/\mu_{\rm H}}$ is the sound speed in the H II region (Hosokawa & Inutsuka 2006). Equation (10) differs from the well-known expansion law given by Spitzer (1978) by a factor of $\sqrt{4/3}$, but it actually provides the better approximation as proven by RHD numerical simulations (e.g. Bisbas et al. 2015; Kim et al. 2017; Williams et al. 2018). Note that equation (10) is basically the same as that given by Kim et al. (2016) but we only consider the thermal pressure of the photoionized gas. Haworth et al. (2015) performed RHD simulations of an expanding H II region by taking into account the microphysics, such as detailed thermal processes and chemistry. They showed that the expansion is slightly delayed by the order of 10 per cent at most. It is reasonable to use equation (10) in our calculation.

2.3 Thermal and chemical structure of photodissociation regions

For every snapshot of an expanding H II region within the cloud, we calculate the thermal and chemical structure in the surrounding PDR. Below, we consider the following seven chemical species: e^-, H^+, H^0, H_2, C^+, O^0 and CO. We assume the total abundance of C and O atoms as $x_{\rm C} = 3.0 \times 10^{-4}$ and $x_{\rm O} = 4.6 \times 10^{-4}$ (Wolfire et al. 1995), where x denotes the number fraction relative to the hydrogen nuclei.

2.3.1 *One-zone thermal and chemical equilibrium model*

We make use of the one-zone modelling of the thermal and chemical equilibrium state of the interstellar medium (e.g. Wolfire et al. 1995; Koyama & Inutsuka 2000). Consider the gas with a given density n exposed by a FUV radiation field with G_0. We determine the unknown variables, the gas temperature T and chemical number fractions $x_{\rm H^+}$, $x_{\rm H_2}$, $x_{\rm CO}$, by solving the following equations

$$\frac{{\rm d}e}{{\rm d}t} = \Gamma(n, T, x^*) - \Lambda(n, T, x^*); \tag{11}$$

$$\frac{{\rm d}x_{\rm H^+}}{{\rm d}t} = R_{\rm H^+}^{\rm form}(n, T, x^*) - R_{\rm H^+}^{\rm rec}(n, T, x^*); \tag{12}$$

$$\frac{{\rm d}x_{\rm H_2}}{{\rm d}t} = R_{\rm H_2}^{\rm form}(n, T, x^*) - R_{\rm H_2}^{\rm dis}(n, T, x^*); \tag{13}$$

Table 2. The thermal and chemical processes included in our model. The references are as follows: (1) Bakes & Tielens (1994); (2) Wolfire et al. (1995); (3) Hollenbach & McKee (1979); (4) Spitzer (1978); (5) McKee et al. (1982); (6) Hollenbach & McKee (1989); (7) Osterbrock (1989); (8) Tielens & Hollenbach (1985); (9) Draine & Bertoldi (1996); (10) Langer (1976); (11) Nelson & Langer (1997).

	Processes	Reference
Heating $\Gamma(n, T, x^*)$	Photoelectric heating	1
	Ionization by soft X-ray	2
	H_2 photodissociation	3
	H_2 formation	3
Cooling $\Lambda(n, T, x^*)$	Fine structure line emission	
	[C II] 158 μm	3
	[O I] 63 μm, 44.2 μm, 145.6 μm	3
	Lyα line emission	4
	CO rotational line emission	5
	Collision with dust grains	6
$R^{H^+}_{form}(n, T, x^*)$	Ionization by soft X-ray	2
$R^{H^+}_{rec}(n, T, x^*)$	Case B recombination	7
$R^{H_2}_{form}(n, T, x^*)$	Dust catalysis	8
	Associative detachment	3
$R^{H_2}_{dis}(n, T, x^*)$	Photodissociation	8,9
	Dust collision	8
$R^{CO}_{form}(n, T, x^*)$	CO formation	10, 11
$R^{CO}_{dis}(n, T, x^*)$	Photodissociation	10, 11

$$\frac{dx_{CO}}{dt} = R^{form}_{CO}(n, T, x^*) - R^{dis}_{CO}(n, T, x^*). \quad (14)$$

Here, e is the internal energy of the gas, Γ and Λ are the heating and cooling rates, and x^* represents $(x_{H^+}, x_{H_2}, x_{CO})$. In the present study, we only consider C^+ and CO as carbon compounds and thus we set $x_{C^+} = x_C - x_{CO}$.

Table 2 presents a full list of thermal and chemical processes associated with the terms on the right-hand side of equations (11)–(14). We only briefly describe some of them. Those readers who are interested in more details can refer to the references therein. For the heating processes, we incorporate the photoelectric emission from grains and H_2 dissociation by the FUV radiation, ionization by the background soft X-ray radiation, and H_2 formation releasing the binding energy. The radiative cooling is primarily caused via the line emission of [C II], [O I], Lyα and CO. We assume the optically thin limit for these line emissions. It is equivalent to ignoring the trapping effect, for which possible effects on our conclusions are discussed in Section 4.2. To avoid overcooling, we set the minimum gas temperature to be 8 K. Regarding the formation of CO molecules, we adopt the simple method given by Nelson & Langer (1997), where CO molecules are approximately formed from C^+ ions and O atoms. Gong et al. (2018) pointed out that the Nelson & Langer (1999) chemical network significantly underestimates CO abundance for $n \lesssim 500$ cm^{-3} and $A_V < 5$. However, we use the chemical network by Nelson & Langer in the present study, as we focus on the CO abundance at a dense shell where $n > 10^4$ cm^{-3}. We also assume the constant dust temperature $T_d = 8$ K for all cases considered. The dust temperature is used to estimate the reformation rate of H_2 molecules and the thermal gas–dust coupling rate via collisions. We also investigate in Section 4.2 the effects of varying T_d in our calculations.

2.3.2 *Time-evolution of a multizone structure*

We calculate the spatial variation of the thermal and chemical state in the PDR around an H II region by repeating the one-zone calculations as follows. At a given time $t = t_j$, the radius and mass of the shell, $M_{sh}(t_j)$ and $r_{sh}(t_j)$, are described by equations (6) and (10). By setting radial grids, we discretize the outer PDR including the shell into cells with the column density $\Delta N_H \sim 10^{19}$ cm^{-2} for each, which corresponds to $A_V = 5.0 \times 10^{-3}$ with the conversion law of $A_V = 5.0 \times 10^{-22} N_H$. The number of the grids is typically ∼1000. The distance from the ionization front to the ith grid r_i is

$$r_i = r_{IF}(t_j) + \sum_{k=0}^{i} \Delta N_H / n_k, \quad (15)$$

which corresponds to the dust optical depth in the outward direction

$$\tau_{in,i} = \sigma_d \sum_{k=0}^{i} \Delta N_H, \quad (16)$$

and the dust optical depth from the edge of the cloud $\tau_{out,i}$

$$\tau_{out,i} = \sigma_d \sum_{k=i}^{N} \Delta N_H. \quad (17)$$

The normalized FUV flux at $r = r_i$ is written as

$$G_i = \frac{1}{F_H} \frac{S_{FUV}}{4\pi r_i^2} \exp(-\tau_{in}, i) + G_{bg} \exp(-\tau_{out,i}), \quad (18)$$

where N is the total number of the grids, $\sigma_d = 10^{-21}$ cm^{2}H^{-1} is the absorption cross-section by dust grains per hydrogen nucleus, and $F_H = 1.21 \times 10^7$ cm^{-2}s^{-1} is the normalization factor that represents the background field near the Solar system (the so-called Habing unit; Habing 1968; Draine & Bertoldi 1996). The last term of unity in equation (18) represents this background exactly. The mass summation over the cells located at $r \le r_i$ is

$$M_i = \sum_{k=0}^{i} 4\pi r_k^2 \mu_H \Delta N_H. \quad (19)$$

By comparing M_i to the total shell mass M_{sh}, we judge whether the ith cell is still within the shell or not. As far as $M_i < M_{sh}$, the cell is regarded as a part of the shell. We determine the thermal and chemical states of such cells in an iterative manner as follows. We assume that the gas pressure within the shell is equal to that of the H II region, $P_{th} = 2 n_{H II} k_B T_{H II}$. So we initially provide the pressure instead of the density in a one-zone calculation, unlike in Section 2.3.1. With the given pressure P_{th} and FUV field G_i, we calculate the unknown variable (T_i, x_i^*) by solving equations (11)–(14) so that the resulting pressure $P_{sh} = n_i(1 + x_{e^-} - x_{H_2}/2) k_B T_i$ matches P_{th}. By doing this, we also determine the number density n_i as well as (T_i, x_i^*). Once (n_i, T_i, x_i^*) are fixed, we then move on to the next $(i + 1)$th cell and repeat the same procedures. If M_i exceeds M_{sh}, the following cells are considered to be outside of the shell as the unshocked ambient gas. We use exactly the same method as in Section 2.3.1 for such cells; we calculate (T_i, x_i^*) for the given number density $n_0(1 - \varepsilon)$ and FUV field G_i. We continue the calculations until reaching the cloud edge, i.e. for $M_i < M_{gas} = M_{cl}(1 - \varepsilon) - M_{H II}$.

2.4 Cloud disruption criteria

To determine the minimum SFE of the cloud, we need some criteria for the cloud disruption, as in Kim et al. (2016). We investigate the effects of the FUV feedback on top of the EUV feedback previously

studied. So, first we use the exactly the same criterion as in Kim et al. (2016).

Criterion 1 (EUV feedback). An H II region and shell are assumed to expand as far as the shell velocity $v_{\rm sh}$ is larger than the critical velocity $v_{\rm bind} = \sqrt{GM_{\rm cl}(1+\varepsilon)/R_{\rm cl}}$,

$$v_{\rm bind} \simeq 5\ {\rm km\ s^{-1}} \left(\frac{M_{\rm cl}}{10^5\ {\rm M_\odot}}\right)^{1/4} \left(\frac{\Sigma_{\rm cl}}{10^2\ {\rm M_\odot\ pc^{-2}}}\right)^{1/4} (1+\varepsilon)^{1/2}. \quad (20)$$

If the trial value of ε is too small, the expansion stalls well before the shell reaches the cloud edge. We iteratively increase ε until $v_{\rm sh} = v_{\rm bind}$ is satisfied at the cloud edge (i.e. $r = R_{\rm cl}$). This gives the minimum SFE.

Note that the above criterion is not the only criterion investigated in Kim et al. (2016). They have also adopted other criteria, showing that the obtained minimum SFE does not largely change. Because our aim is to study the effects of FUV radiation, we only focus on one representative case.

Criterion 2 (FUV feedback). We assume that star formation is suppressed in a warm PDR, where the gas temperature is above the threshold value of 100 K. Technically, if the trial value of ε is too small, the temperature outside the shell is at least partly lower than 100 K. We iteratively increase ε until the gas is heated above 100 K everywhere outside the shell at a certain epoch. This gives the minimum SFE.

Although the temperature is raised to ∼100–1000 K in the PDR, the corresponding sound speed is much smaller than that of the photoionized gas. Therefore, as often presumed, the resulting FUV feedback should be weaker than the EUV feedback. The FUV effects would not operate to disrupt the entire structure of the molecular clouds. We suppose that the star formation in the PDR is locally hindered with the lack of cold (∼10 K) materials. Because the exact strength of the FUV feedback is uncertain, we also consider Criterion 1 for limiting the SFEs. We only estimate effects of FUV feedback on the chemical compositions of cloud remnants for such cases.

3 RESULTS

3.1 Time evolution of thermal and chemical structure

First, we present typical evolution of the thermal and chemical structure in the PDR around an H II region. Here we spotlight one particular case with the molecular cloud mass $M_{\rm cl} = 10^4\ {\rm M_\odot}$ and surface density $\Sigma_{\rm cl} = 300\ {\rm M_\odot\ pc^{-2}}$. We follow the evolution with a star cluster with $M_* = \varepsilon_{\rm min} M_{\rm cl} \simeq 1220\ {\rm M_\odot}$ formed at the cloud centre.[1] The corresponding stellar EUV and FUV photon number luminosities are $S_{\rm EUV} \simeq 4.2 \times 10^{49}\ {\rm sec^{-1}}$ and $S_{\rm FUV} \simeq 8.0 \times 10^{49}\ {\rm sec^{-1}}$ respectively.

Fig. 1 shows the position of ionization front $r_{\rm IF}$ (equation 10) and shell $r_{\rm sh} = r_{\rm IF} + \sum \Delta N_{\rm H}/n_i$ as a function of time. Fig. 2 shows the time evolution of the 1D thermal and chemical structure at (a) $t = 0$, (b) $t = 0.5\, t_{R_{\rm cl}}$, and (c) $t = t_{R_{\rm cl}}$, where $t_{R_{\rm cl}}$ is the time when the shell reaches the cloud edge. Note that the total column density deceases with time in this figure. This is explained by the difference of the geometry: the initial and final column density $N_0 = n_0 R_{\rm cl}$ and $N_{\rm H}^{\rm shell}$ are related as

$$M_{\rm gas} = \frac{4}{3}\pi R_{\rm cl}^2 N_0 \mu_{\rm H} \sim 4\pi R_{\rm cl}^2 N_{\rm H}^{\rm shell} \mu_{\rm H}, \quad (21)$$

[1]For this representive case, we find that the minimum SFE $\varepsilon \simeq 0.12$ is insensitive to the choice of cloud disruption criteria (see also Section 3.2).

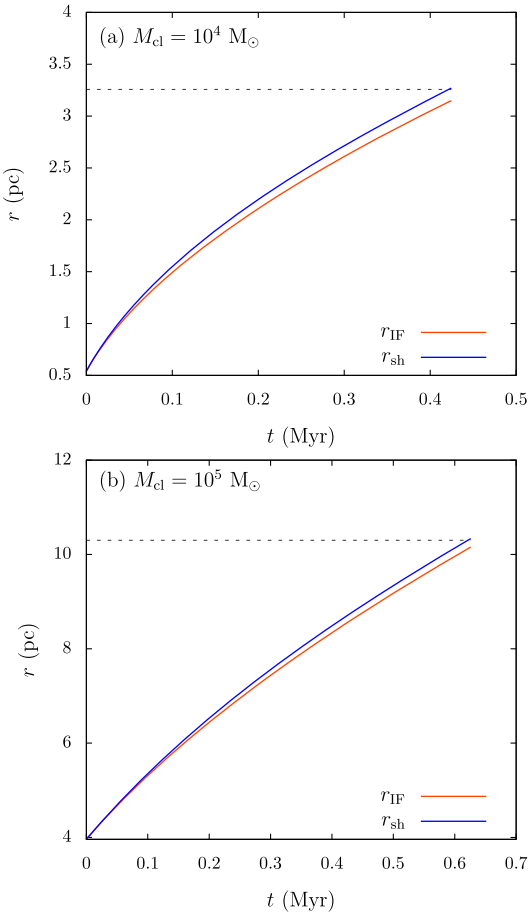

Figure 1. The positions of the ionization front $r_{\rm IF}$ (red solid line) and the shock front $r_{\rm sh}$ (blue solid line) as functions of time for (a) $M_{\rm cl} = 10^4\ {\rm M_\odot}$ ($\Sigma_{\rm cl} = 300\ {\rm M_\odot\ pc^{-2}}$) and (b) $M_{\rm cl} = 10^5\ {\rm M_\odot}$ ($\Sigma_{\rm cl} = 300\ {\rm M_\odot\ pc^{-2}}$). The black dashed line in each panel indicates the position of the outer edge of the cloud: (a) $R_{\rm cl} = 3.25$ pc; (b) $R_{\rm cl} = 10.3$ pc.

where we approximate $r_{\rm IF}(t_{R_{\rm cl}})$ as $R_{\rm cl}$. Then we find $N_{\rm H}^{\rm shell} \sim N_0/3$.

Fig. 2(a) presents the snapshot at $t = 0$, when the initial Strömgren sphere is created. Because, at this epoch, the shell has not appeared yet, the density is constant everywhere. The temperature rapidly grows toward the central cluster because of the efficient photoelectric heating by the strong stellar FUV radiation. In the outer part with $1.2 \times 10^{22} \lesssim N_{\rm H} \lesssim 1.8 \times 10^{22}\ {\rm cm^{-2}}$, however, the temperature profile is flat as we set the minimum gas temperature to 8 K (see Section 2.3.1). In the lower panel, we see that the hydrogen molecules are dissociated by the cluster FUV radiation for $N_{\rm H} \lesssim 4.0 \times 10^{21}\ {\rm cm^{-2}}$.

Fig. 2(b) shows that the swept-up shell has emerged by the epoch of $t = 0.5\, t_{R_{\rm cl}}$ and $r_{\rm IF} = 2.2$ pc. The discontinuity of physical quantities at $N_{\rm H} \simeq 5.4 \times 10^{21}\ {\rm cm^{-2}}$ corresponds to the preceding shock front, or the shell outer edge represented by $r_{\rm sh}$. Within the shell, the temperature decreases outward as the FUV flux drops as a result of the dust attenuation. The density inversely increases, because the thermal pressure is assumed to be fixed at the value of the H II region. The hydrogen dissociation front is shifted to a lower column density at $N_{\rm H} \simeq 2.5 \times 10^{21}\ {\rm cm^{-2}}$ than in Fig. 2(a) because of the efficient self-shielding of H_2 molecules within the dense shell. By contrast, there is only a small amount of CO molecules within the shell. The temperature just outside the shell is slightly higher than that inside the shell because the [C II] line emission, which is the dominant

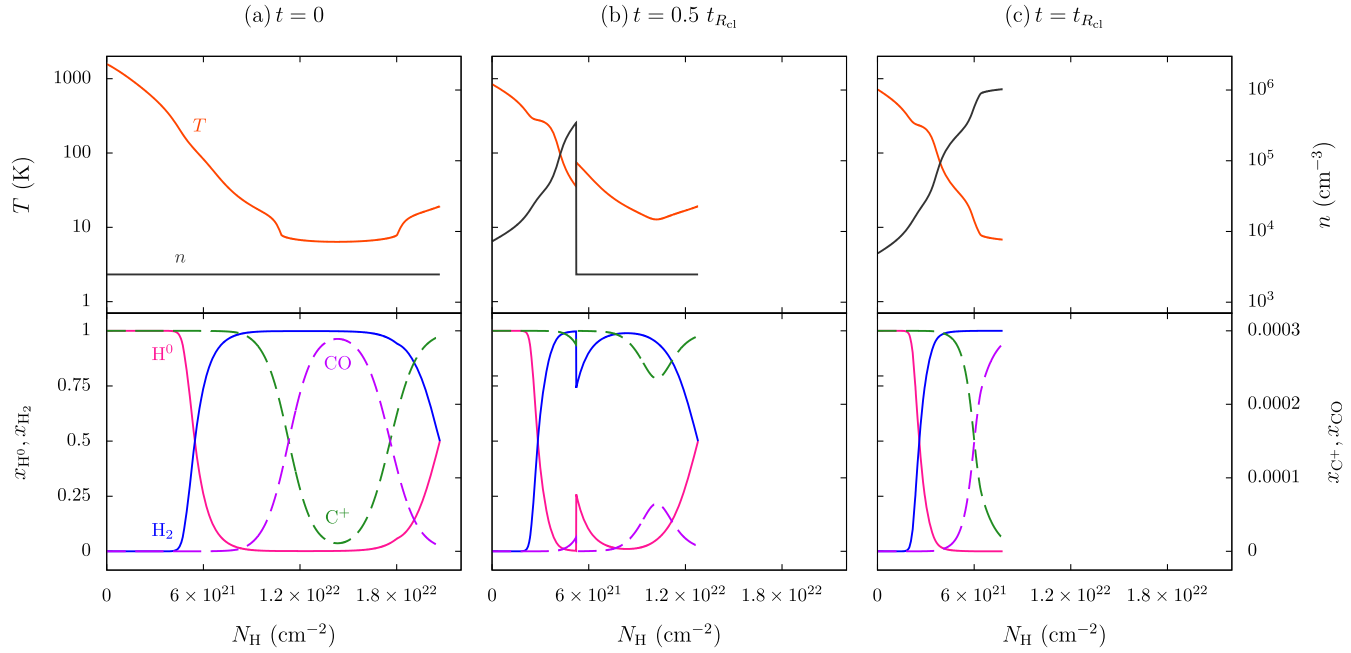

Figure 2. Time evolution of the thermal and chemical structure in the PDR around an H II region. The cloud mass and surface density are $M_{\rm cl} = 10^4$ M$_\odot$ and $\Sigma_{\rm cl} = 300$ M$_\odot$ pc^{-2} for this case. The panels show the snapshots at the different epochs of (a) $t = 0$, (b) $t = 0.5\,t_{R_{\rm cl}}$ and (c) $t = t_{R_{\rm cl}}$, where $t_{R_{\rm cl}}$ is the time when the shell reaches the cloud edge. The horizontal axis denotes the column density of hydrogen nuclei measured from the ionization front; that is, $N_{\rm H} = 0$ corresponds to $r_{\rm IF}$ and the maximum value of $N_{\rm H}$ corresponds to $R_{\rm cl}$. Top: the gas temperature (red line) and density (grey line) are plotted, for which the scaling is presented with the left- and right-hand axes. Bottom: the fractional abundances of H I (red solid line), H_2 (blue solid line), C II (green dashed line) and CO (purple dashed line) are plotted. The left-hand (right-hand) axis is used for scaling of H I and H_2 (C II and CO) abundances.

coolant of the cloud, is less efficient with a lower density (see also Section 3.2.2). As the density differs by approximately two orders of magnitude across the shock front, the cooling efficiency also differs.

Fig. 2(c) shows the final snapshot for the current case, when all of the cloud materials are swept into the shell. Unlike the previous snapshot, the CO dissociation front is taken into the shell at $N_{\rm H} \simeq 6.0 \times 10^{21}$ cm^{-2} because the shell column density has become so large that CO molecules are protected against the cluster FUV radiation with the dust attenuation. As shown below, this is the final snapshot when the minimum SFE is determined, and the swept-up gas on the shell is, so to speak, the remnant of the molecular cloud. It is evident that the chemical composition of such a cloud remnant is not homogeneous. There are some H_2 molecules, but only a small number of these are associated with CO molecules. We return to this point later in Section 3.3.

Next, we show the case where CO molecules are almost completely destroyed by FUV radiation. Fig. 3 represents the case with $M_{\rm cl} = 10^5$ M$_\odot$ and $\Sigma_{\rm cl} = 300$ M$_\odot$ pc^{-2}. The central cluster mass is 2.6×10^4 M$_\odot$ and the corresponding stellar EUV and FUV photon number luminosity is $S_{\rm EUV} \simeq 1.2 \times 10^{51}$ s^{-1} and $S_{\rm FUV} \simeq 2.5 \times 10^{51}$ s^{-1}, respectively. The clear difference from the case with $M_{\rm cl} = 10^4$ M$_\odot$ is that CO molecules do not survive throughout the time evolution. This behaviour is mainly explained by the difference of G_0 (see Section 3.3 for a detailed discussion).

3.2 Star formation efficiency of molecular clouds

3.2.1 Limiting star formation efficiency by FUV radiation

In this section, we investigate the SFE of the molecular clouds set by the EUV and FUV feedback effects. Consider an expanding H II region and surrounding PDR around a newly born cluster in a given molecular cloud. If the cluster is not sufficiently massive (or luminous), only a small part of the cloud near the cluster would be affected by the feedback; further star formation would occur in the remnant part until enough stars have formed to halt further star formation and destroy the whole cloud. Hence, there should be a minimum value of the SFE $\varepsilon_{\rm min}$ above which the cloud is destroyed by radiative feedback. We calculate $\varepsilon_{\rm min}$ as a function of $M_{\rm cl}$ and $\Sigma_{\rm cl}$ in the iterative manner as outlined in Section 2.1.

Each panel in Fig. 4 shows the minimum SFE obtained as a function of the cloud surface density $\Sigma_{\rm cl}$ for the same mass $M_{\rm cl}$. The cloud masses of $M_{\rm cl} = 10^4$, 10^5 and 10^6 M$_\odot$ are assumed for Figs 4(a), (b) and (c), respectively.

The grey line in each panel represents the case where only the EUV feedback is considered (Criterion 1, $\varepsilon_{\rm min,1}$). We see that $\varepsilon_{\rm min,1}$ is an increasing function of $\Sigma_{\rm cl}$, as shown in Kim et al. (2016). Such a behaviour is well understood by considering the $\Sigma_{\rm cl}$ dependences of the cloud radius $R_{\rm cl}$ and the initial Strömgren radius $r_{\rm St,0}$: $R_{\rm cl} \propto \Sigma_{\rm cl}^{-1/2}$ and $r_{\rm St,0} \propto \Sigma_{\rm cl}^{-1}$ for a given $M_{\rm cl}$ and $S_{\rm EUV}$. This means that, with increasing $\Sigma_{\rm cl}$, the typical size of the H II region $r_{\rm St,0}$ relative to the cloud size $R_{\rm cl}$ decreases. The more massive or luminous cluster is necessary for the H II region to cover the whole cloud for such a case. Thus, the resulting $\varepsilon_{\rm min}$ is higher for higher surface density. Kim et al. (2016) provide the analytical formula describing this dependence as

$$\frac{\varepsilon_{\rm min}}{(1-\varepsilon_{\rm min}^2)^2} = \left(\frac{\pi^{5/4} G}{\eta_{\rm th} \mathcal{T}}\right)^2 M_{\rm cl}^{1/2} \Sigma_{\rm cl}^{5/2}, \tag{22}$$

where $\eta_{\rm th} = 9/4$ and $\mathcal{T} = 8\pi k_{\rm B} T_{\rm H\,II} [3 f_{\rm ion} \Xi_{\rm EUV} / 4\pi\alpha_{\rm B}]^{1/2}$. Note that the grey line in each panel representing the EUV feedback is not identical because of the dependence of $\varepsilon_{\rm min} \propto M_{\rm cl}^{1/2}$ in equation (22).

In our model, the gas density is proportional to $(1 - \varepsilon)$ and the photon number flux $S_{\rm EUV}$ is proportional to ε, so that the size of the

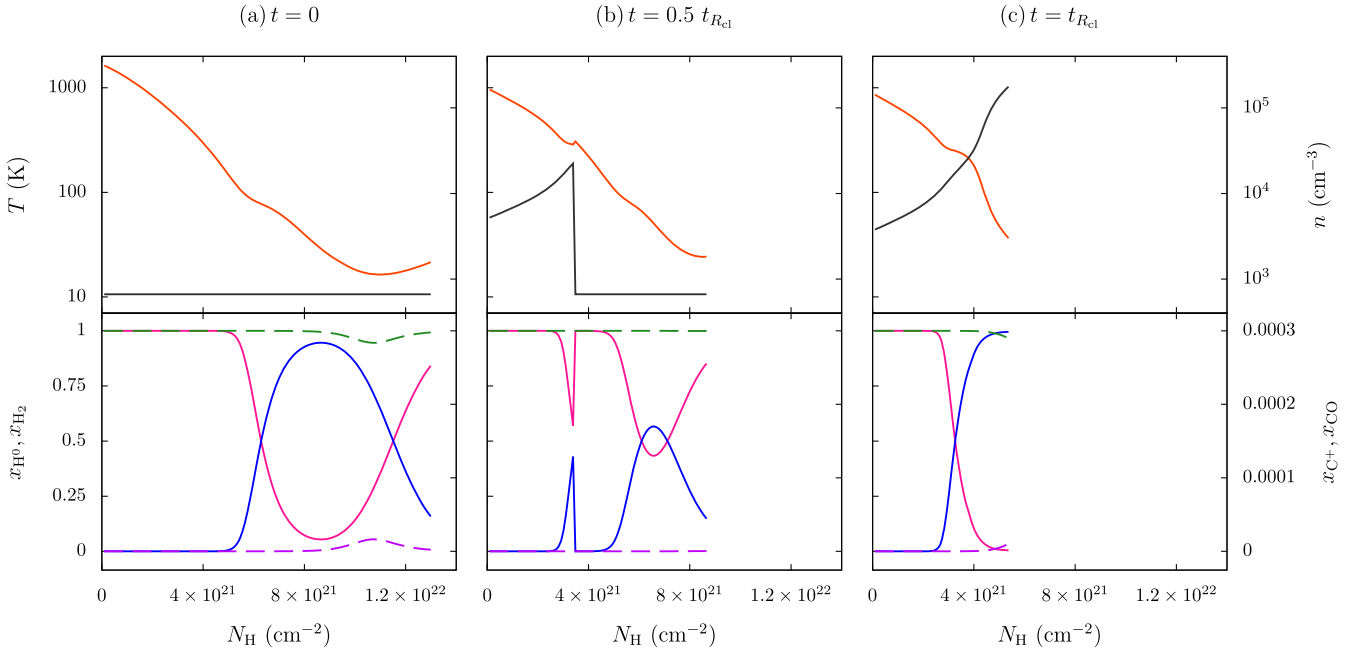

Figure 3. Same as Fig. 2, except for the higher cloud mass of $M_{\rm cl} = 10^5$ M$_\odot$ and surface density $\Sigma_{\rm cl} = 300$ M$_\odot$ pc^{-2}.

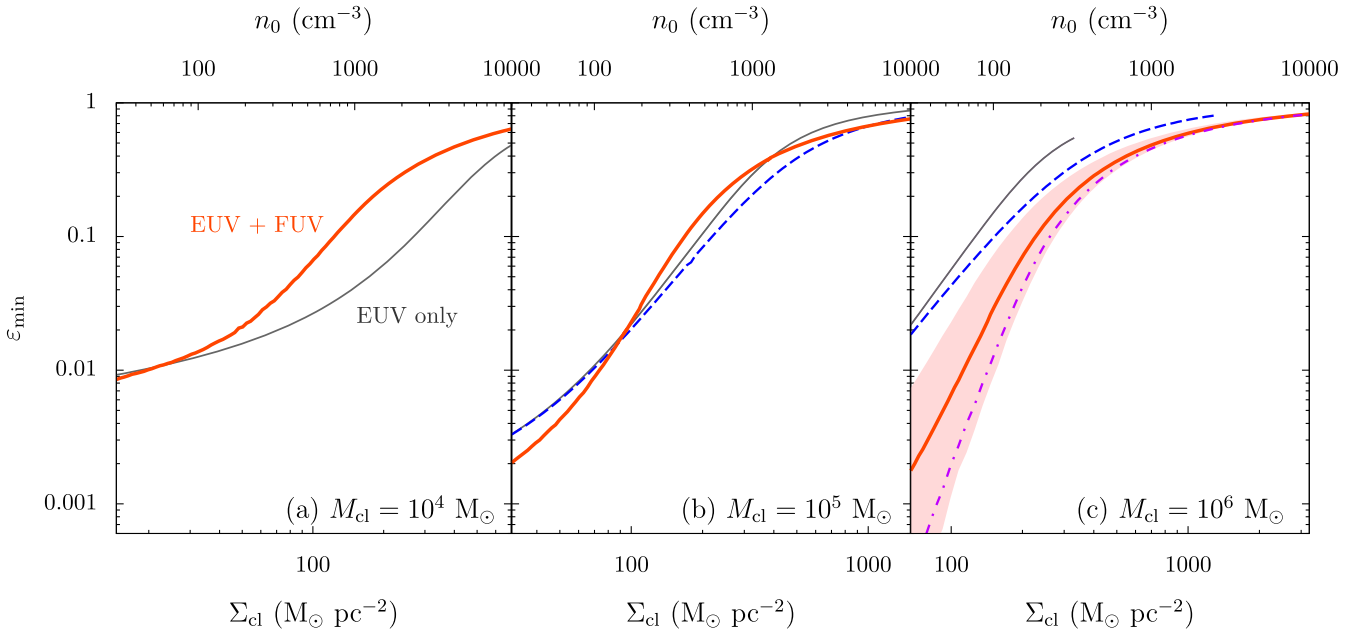

Figure 4. The minimum SFE $\varepsilon_{\rm min}$ calculated as a function of the cloud surface density $\Sigma_{\rm cl}$. The different cloud masses of $M_{\rm cl} = 10^4$ M$_\odot$, $M_{\rm cl} = 10^5$ M$_\odot$ and $M_{\rm cl} = 10^6$ M$_\odot$ are assumed for panels (a), (b) and (c). In each panel, the thick red line represents the case where the SFE is limited by both EUV and FUV feedback (Criterion 2). The black line represents the reference case only with the EUV feedback (Criterion 1), as considered in Kim et al. (2016). The blue dashed lines in panels (b) and (c) represent the cases where the effects of the radiation pressure are included for the dynamics of the H II region expansion. In panel (c), the red shaded zone represents the range where the threshold temperature is varied between 50 and 300 K in Criterion 2, and the purple dot-dashed line represents the case with lower C and O abundances, $x_{\rm C} = 1.4 \times 10^{-4}$ (Cardelli et al. 1996) and $x_{\rm O} = 2.8 \times 10^{-4}$ (Cartledge et al. 2004). Note that each panel shows a different range of $\Sigma_{\rm cl}$.

initial H II region becomes increasingly larger for higher ε. Thus, there is a critical ε over which $r_{\rm IF,0} \geq R_{\rm cl}$. This occurs when the cloud surface density and mass are both large (see also Kim et al. 2016). This explains why the grey solid line stops in the middle of Fig. 4(c).

Let us next examine the effect of the FUV radiation on limiting the minimum SFE. The red line in each panel of Fig. 4 represents the cases with FUV feedback (i.e. Criterion 2, $\varepsilon_{\rm min,2}$). Comparing the red line with the grey line, we can evaluate the effect of FUV feedback on top of EUV feedback. The minimum SFE is defined as $\varepsilon_{\rm min} = \min(\varepsilon_{\rm min,1}, \varepsilon_{\rm min,2})$.

Fig. 4(a) shows that the introduction of FUV feedback does not change the SFEs in the cases with cloud mass $M_{\rm cl} = 10^4$ M$_\odot$; $\varepsilon_{\rm min} =$

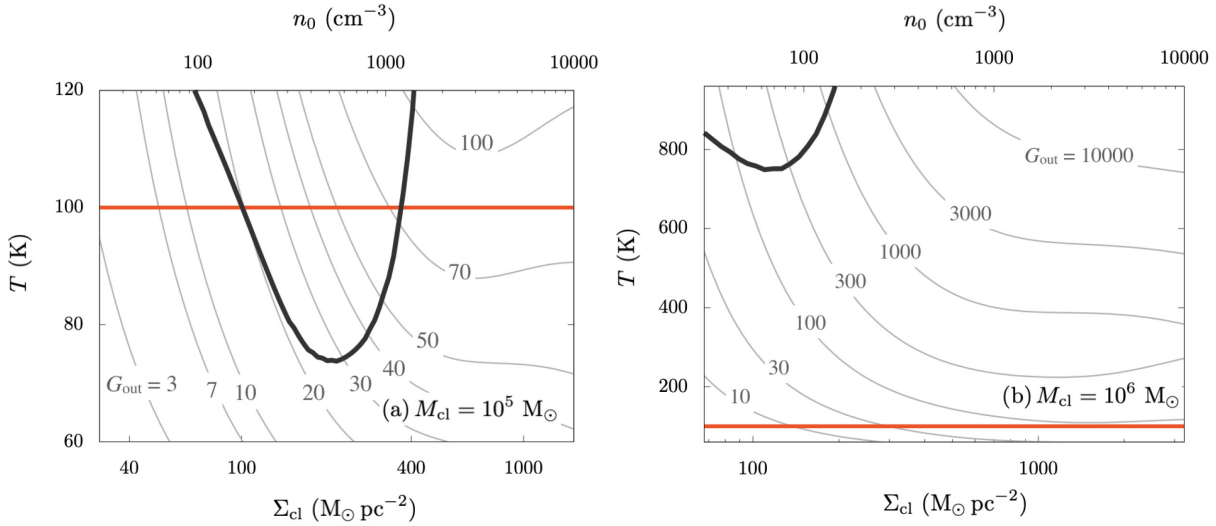

Figure 5. Effects of FUV heating in limiting the minimum SFE with $M_{\rm cl} = 10^5$ M$_\odot$ (a) and $M_{\rm cl} = 10^6$ M$_\odot$ (b). In each panel, the thick black line represents the gas temperature at the cloud's outer edge when the minimum SFE is determined only by EUV feedback (Criterion 1, the grey lines in Fig. 4). In such a case, an expanding H II region and surrounding shell just fill the whole cloud, and the 'cloud edge' corresponds to the unshocked gas just outside the shell. The red line represents the critical temperature 100 K, above which the star formation is assumed to be suppressed by FUV feedback (Criterion 2). At $\Sigma_{\rm cl}$ for which the red curve exceeds the red line, the gas is heated up above 100 K before the shell reaches the cloud edge, meaning that the SFE should be primarily limited by the FUV feedback if included. The grey contours denote the equilibrium temperature for different values of FUV flux $G_{\rm out}$ as a function of the density. We note that, in panel (b), the vertical axis covers the much larger range of the temperature than in panel (a).

$\varepsilon_{\rm min,1}$. For more massive clouds with $M_{\rm cl} = 10^6$ M$_\odot$ (Fig. 4c), in contrast, the FUV feedback is quite important; $\varepsilon_{\rm min} = \varepsilon_{\rm min,2}$. For a given $\Sigma_{\rm cl}$, the minimum SFE is reduced by the inclusion of FUV feedback by one order of magnitude, at maximum. In particular, the difference is larger at smaller surface density, $\Sigma_{\rm cl}$. In the case with intermediate mass of $M_{\rm cl} = 10^5$ M$_\odot$ (Fig. 4b), the resulting $\varepsilon_{\rm min}$ is only slightly (by about 10 per cent) reduced by the FUV feedback effect at the lower and higher ends of $\Sigma_{\rm cl}$ (i.e. $\Sigma_{\rm cl} \lesssim 100$ M$_\odot$ pc^{-2} and $\Sigma_{\rm cl} \gtrsim 400$ M$_\odot$ pc^{-2}).

We also study the parameter dependences of SFEs in the case with cloud mass $M_{\rm cl} = 10^6$ M$_\odot$, where the effect of FUV feedback is the most remarkable. We consider the different threshold temperatures between 50 and 300 K, and lower abundances of carbon and oxygen (e.g. Cardelli et al. 1996; Cartledge et al. 2004). We find that the variations of SFE are the most visible when the surface density is low, and the differences amount to a factor of 10 at most. However, the overall trend remains the same, irrespective of parameter values.

To summarize, the FUV feedback is sufficiently effective in massive and low surface density clouds. We further analyse our calculations to interpret the results in Section 3.2.2.

3.2.2 Interpreting the results

As shown in Section 3.2.1, the effects of FUV feedback on limiting the minimum SFE depend on the cloud parameters, such as the cloud mass $M_{\rm cl}$ and surface density $\Sigma_{\rm cl}$. Here we look into our results further, to consider what causes such variations.

First, we investigate the case of clouds with $M_{\rm cl} = 10^5$ M$_\odot$. Because the heating in PDRs is assumed to limit the SFE, we consider the temperature just outside the shell, $T_{\rm out}$. The thick black line in Fig. 5(a) shows $T_{\rm out}$ as a function of $\Sigma_{\rm cl}$ at the cloud edge $r = R_{\rm cl}$ at $t = t_{R_{\rm cl}}$, when the SFE is determined by the EUV feedback only (Criterion 1). We see that $T_{\rm out}$ has the local minimum at $\Sigma_{\rm cl} \simeq 200$ M$_\odot$ pc^{-2}. As the PDR is primarily heated up via the photoelectric emission from grains, the local FUV flux $G_{\rm out}$ is a key quantity to determine $T_{\rm out}$. According to equations (1) and (18), $G_{\rm out}$ is proportional to $S_{\rm FUV}\Sigma_{\rm cl}/M_{\rm cl} \propto \varepsilon_{\rm min}\Sigma_{\rm cl}$ (neglecting dust attenuation). It follows that $G_{\rm out}$ monotonically increases with increasing $\Sigma_{\rm cl}$, because the minimum SFE or $S_{\rm FUV}$ increases with $\Sigma_{\rm cl}$ (Fig. 4a). With the above facts, one may ask why $T_{\rm out}$ decreases with $\Sigma_{\rm cl}$ for $\Sigma_{\rm cl} \lesssim 200$ M$_\odot$ pc^{-2}, whereas $G_{\rm out}$ increases with $\Sigma_{\rm cl}$. This is explained by the nature of the [C II] line cooling, which dominates over other processes. The [C II] cooling rapidly becomes efficient with the increasing density n (or $\Sigma_{\rm cl}$) for $n \ll n_{\rm cr} \simeq 2000$ cm^{-3}. Such a trend is illustrated as grey lines in Fig. 5, which show the equilibrium gas temperature as a function of density for different values of $G_{\rm out}$, clearly showing such a trend. The slopes of the contour lines are so steep that $T_{\rm out}$ drops while $G_{\rm out}$ increases with $\Sigma_{\rm cl}$.

Let us compare $T_{\rm out}$ with the threshold temperature for the FUV feedback, 100 K. We see that $T_{\rm out}$ exceeds 100 K in both the lower and higher sides of $\Sigma_{\rm cl}$. It suggests that the destruction by FUV feedback is more effective than dynamical disruption. Because the temperature becomes lower with lower $G_{\rm out}$ at a given $\Sigma_{\rm cl}$, only the smaller $S_{\rm FUV}$ (or smaller ε) is enough to realize $T_{\rm out} = 100$ K. This explains why ε is reduced by FUV feedback in the higher and lower sides of $\Sigma_{\rm cl}$ in Fig. 4.

Fig. 5(b) shows the same plots as Fig. 5(a) but for the cases with more massive clouds with $M_{\rm cl} = 10^6$ M$_\odot$, where the FUV feedback effects are more remarkable than other cases. In this case, $T_{\rm out}$ is much higher than the threshold temperature 100 K for any range of $\Sigma_{\rm cl}$. This is due to the dependence of $G_{\rm out} \propto S_{\rm FUV}\Sigma_{\rm cl}/M_{\rm cl}$ again. With a fixed value of $\Sigma_{\rm cl}$, $G_{\rm out}$ is larger with higher $M_{\rm cl}$ because $G_{\rm out} \propto \varepsilon S_{\rm FUV}/M_* = \varepsilon\Xi_{\rm FUV}$ and ε is enhanced following equation (22). The SFE required to disrupt the natal cloud is much smaller than the case only with EUV feedback. Fig. 5(b) also suggests that even with a large threshold temperature $\lesssim$700 K, the FUV feedback should still reduce the minimum SFE $\varepsilon_{\rm min}$.

3.3 Chemical compositions of molecular cloud remnants

Our calculations suggest that the EUV and FUV radiative feedback from forming clusters jointly contribute to reduce the SFE of molecular clouds. In this section, we cast light on the gas that has not been used for star formation (i.e. the 'remnants' of the clouds). The cloud remnants still retain a large part of the cloud materials because the obtained SFEs are much smaller than unity for many cases. We focus on the chemical compositions of the cloud remnants, which are also followed in our calculations.

We calculate the masses of H I, CO-dark and CO-bright H_2 gases as follows:

$$M_{\rm H\,I} = \sum_{k=0}^{N} 4\pi r_k^2 \mu_{\rm H} \Delta N_{\rm H} x_{\rm H^0}; \tag{23}$$

$$M_{\rm H_2\,w/o\,CO} = \sum_{k=0}^{N} 4\pi r_k^2 \mu_{\rm H} \Delta N_{\rm H} x_{\rm H_2} x_{\rm C^+}/x_{\rm C}; \tag{24}$$

$$M_{\rm H_2\,w/\,CO} = \sum_{k=0}^{N} 4\pi r_k^2 \mu_{\rm H} \Delta N_{\rm H} x_{\rm H_2} x_{\rm CO}/x_{\rm C}. \tag{25}$$

First, we consider the cases with the fixed cloud mass $M_{\rm cl} = 10^5$ M$_\odot$. Fig. 6(a) presents the mass fraction of the gas with the different chemical properties as functions of $\Sigma_{\rm cl}$. The neutral and molecular hydrogen are the dominant components of the cloud remnants, and they occupy 70 and 30 per cent of the total mass, respectively. In particular, we distinguish H_2 molecules associated with CO molecules and those without CO. The H_2 gas without CO molecules is the so-called 'CO-dark' molecular gas. Let us look at the cases where the minimum SFE is limited by the EUV and FUV feedback (Criterion 2, solid lines). Fig. 6(a) shows that most of the H_2 molecules contained in the remnants are actually CO-dark. Such a trend only has a weak dependence on $\Sigma_{\rm cl}$; the mass of the CO-dark H_2 gas is generally much less than 10 per cent of that of the H_2 gas associated with CO molecules. This is caused by the different shielding processes of H_2 and CO molecules. As shown in Fig. 6(c), the column density of the shell is roughly $N_{\rm H}^{\rm shell} \simeq 2-7\times10^{21}$ cm^{-2}, corresponding to $A_V \simeq 1$–3.5. The dust attenuation of the FUV radiation is not very efficient for such cases. In fact, Fig. 6(b) shows that the FUV flux at the shock front non-dimensional quantity ($G_{\rm out}$) is several to several tens, which is high enough to photodissociate CO molecules. However, H_2 molecules are protected against the FUV radiation by the self-shielding effect even with the small column densities. As self-shielding is not available for CO molecules, which only have small abundance, CO molecules are selectively destroyed.

We also investigate how the above properties are altered when we only consider the EUV feedback (see the thin symbols connected with dashed lines in Fig. 6). For such cases, only the quantities for $\Sigma_{\rm cl} \gtrsim 300$ M$_\odot$ pc^{-2} are modified. Fig. 6(a) shows that the amount of H_2 with CO molecules is further reduced for such large $\Sigma_{\rm cl}$. Fig. 6(c) explains that it is caused by the decline of the shell column density $N_{\rm H}^{\rm shell}$. We see that $N_{\rm H}^{\rm shell}$ decreases with $\Sigma_{\rm cl}$ for $\Sigma_{\rm cl} \gtrsim 300$ M$_\odot$ pc^{-2}. Fig. 6(b) shows that $G_{\rm out}$ accordingly rises with $\Sigma_{\rm cl}$, resulting in the efficient dissociation of CO molecules.

The above dependence on the feedback criteria is actually well understood with the following analytical arguments. Because the ionized gas density (at $t = t_{R_{\rm cl}}$) is given by

$$n_{\rm H\,II} = \sqrt{\frac{3S_{\rm EUV} f_{\rm ion}}{4\pi R_{\rm cl}^3 \alpha_{\rm B}}}, \tag{26}$$

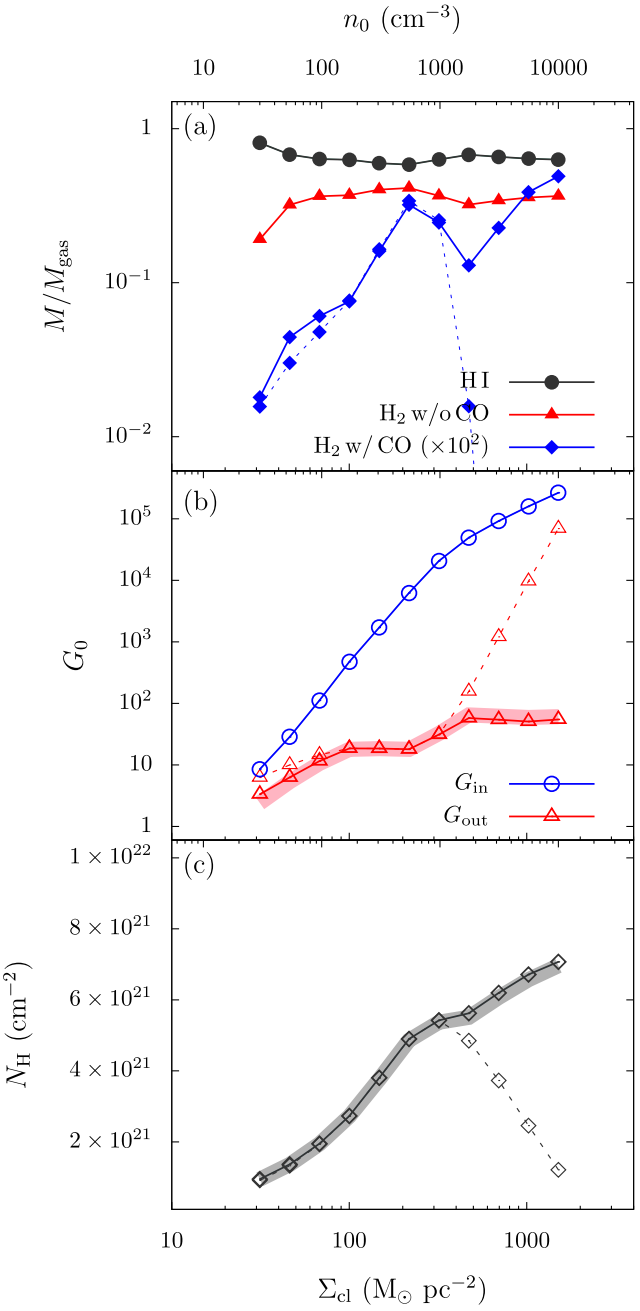

Figure 6. Chemical compositions of the gas that has not been converted into stars (molecular cloud 'remnants', panel a) and relevant quantities (panels b and c). The same cloud mass of $M_{\rm cl} = 10^5$ M$_\odot$ is assumed for the different cloud surface densities $\Sigma_{\rm cl}$ as in Fig. 4. Panel (a) shows the mass fractions relative to the total remnant mass $M_{\rm gas} = M_{\rm cl}(1-\varepsilon) - M_{\rm H\,II}$ for the different chemical properties: H I (black filled circles), H_2 without CO (red filled triangles) and H_2 with CO (blue filled squares). Panel (b) shows FUV fluxes throughout the shell. The blue open circles represent the incident FUV flux at the ionization front, and the red open triangles represent that at the preceding shock front. Panel (c) shows the hydrogen column density of the shell. In each panel, the symbols connected by the solid lines represent the cases where the minimum SFEs are limited by the EUV and FUV feedback. We also show the cases only with EUV feedback using thin symbols connected by dashed lines. In panels (b) and (c), the thick solid lines represent the analytical evaluations of $G_{\rm out}$ and $N_{\rm H}^{\rm shell}$ by equations (30) and (29).

the mass of the ionized gas can be written as

$$M_{\rm H\,II} = \frac{4}{3}\pi R_{\rm cl}^3 \mu_{\rm H} n_{\rm H\,II}$$
$$= \mu_{\rm H}\left(\frac{4 f_{\rm ion}\Xi_{\rm EUV}}{3\alpha_{\rm B}\pi^{1/2}}\right)^{1/2} \varepsilon^{1/2} M_{\rm cl}^{5/4}\Sigma_{\rm cl}^{-3/4} \quad (27)$$
$$= 1.2\times10^4\,{\rm M}_\odot\left(\frac{\varepsilon}{10^{-2}}\right)^{1/2}\left(\frac{M_{\rm cl}}{10^5\,{\rm M}_\odot}\right)^{5/4}$$
$$\times\left(\frac{\Sigma_{\rm cl}}{10^2\,{\rm M}_\odot{\rm pc}^{-2}}\right)^{-3/4}.$$

As the ratio $M_{\rm H\,II}/M_{\rm cl}$ depends only weakly on $M_{\rm cl}$ and $\Sigma_{\rm cl}$, we take $M_{\rm H\,II} \sim 0.1\ M_{\rm cl}$. Then, the shell column density $N_{\rm H}^{\rm shell}$ and FUV flux at the shock front $G_{\rm out}$ obeys the following relations:

$$M_{\rm shell} = M_{\rm cl}(1-\varepsilon) - M_{\rm H\,II} \approx 4\pi R_{\rm cl}^2 \mu_{\rm H} N_{\rm H}^{\rm shell}. \quad (28)$$

That is, we have

$$N_{\rm H}^{\rm shell} = \frac{\Sigma_{\rm cl}}{4\mu_{\rm H}}\left(1-\varepsilon-\frac{M_{\rm H\,II}}{M_{\rm cl}}\right) \sim \frac{\Sigma_{\rm cl}}{4\mu_{\rm H}}(0.9-\varepsilon), \quad (29)$$

$$G_{\rm out} = \frac{1}{F_{\rm H}}\frac{S_{\rm FUV}}{4\pi R_{\rm cl}^2}\exp\left(-\sigma_{\rm d}N_{\rm H}^{\rm shell}\right)$$
$$\sim \frac{\varepsilon\,\Xi_{\rm FUV}}{4F_{\rm H}}\Sigma_{\rm cl}\exp\left[-\frac{\sigma_{\rm d}}{4\mu_{\rm H}}\Sigma_{\rm cl}(0.9-\varepsilon)\right]. \quad (30)$$

The factor of $(0.9-\varepsilon)$ in the above equations is actually important to understand the results. Fig. 4(a) shows that, for $\Sigma_{\rm cl} \gtrsim 300\ {\rm M}_\odot\ {\rm pc}^{-2}$, $\varepsilon_{\rm min}$ only slightly changes with whether the FUV feedback is included or not. Because $\varepsilon_{\rm min}$ is close to 0.9, however, the resulting change of $(0.9-\varepsilon)$ is large. Only with EUV feedback does $(0.9-\varepsilon)$ significantly decline, meaning that there is only a small amount of the remnant gas that shields the FUV radiation. It follows that the shell column density declines for $\Sigma_{\rm cl} \gtrsim 300\ {\rm M}_\odot\ {\rm pc}^{-2}$ for such cases.

We have performed the same analyses as above also for the cases with the different cloud masses $M_{\rm cl} = 10^6\ {\rm M}_\odot$ and $10^4\ {\rm M}_\odot$. Fig. 7 presents the former cases with the large cloud mass $10^6\ {\rm M}_\odot$. Again, most of the hydrogen molecules contained in the cloud remnants are not associated with CO molecules (Fig. 7a). If we only consider the EUV feedback, we can hardly find any CO molecules remaining. The shell column density $N_{\rm H}^{\rm shell}$ is only less than $2\times10^{21}\ {\rm cm}^{-2}$ (Fig. 7b), and the dust attenuation hardly contributes to reduce the FUV flux throughout the remnant gas (Fig. 7c).

Similarly, Fig. 8 presents the cases for low-mass clouds with $M_{\rm cl} = 10^4\ {\rm M}_\odot$. Recall that the minimum SFE does not depend on whether the FUV feedback is considered or not for this case. We see higher fractions of H_2 gas associated with CO molecules than the previous cases, in particular, for $\Sigma_{\rm cl} \gtrsim 300\ {\rm M}_\odot\ {\rm pc}^{-2}$ (Fig. 8a). The above analytical formulae are again useful to interpret such a variation. As $\varepsilon_{\rm min} \ll 1$ for the current cases (see equation 22), the factor of $(0.9-\varepsilon)$ is just regarded as a constant. The combination of equations (29) and (30) leads to $N_{\rm H,shell} \propto \Sigma_{\rm cl}$ and $G_{\rm out} \propto \epsilon\,\Xi_{\rm FUV}\exp(-\Sigma_{\rm cl})$, indicating that the FUV flux rapidly drops with increasing $\Sigma_{\rm cl}$ because the shell column density increases. Indeed, the column density $N_{\rm H,shell}$ monotonically increases with increasing $\Sigma_{\rm cl}$ (Fig. 8c). The FUV flux $G_{\rm out}$ decreases in concert, as predicted by equation (30). For $\Sigma_{\rm cl} \gtrsim 300\,{\rm M}_\odot\,{\rm pc}^{-2}$, $G_{\rm out}$ is just limited by the background value $G_{\rm out} = 1$ (Fig. 8b). The above facts suggest that the FUV radiation from the cluster is substantially attenuated by the dust grains. As a result, a certain amount of CO molecules survives, being protected against the dissociating photons.

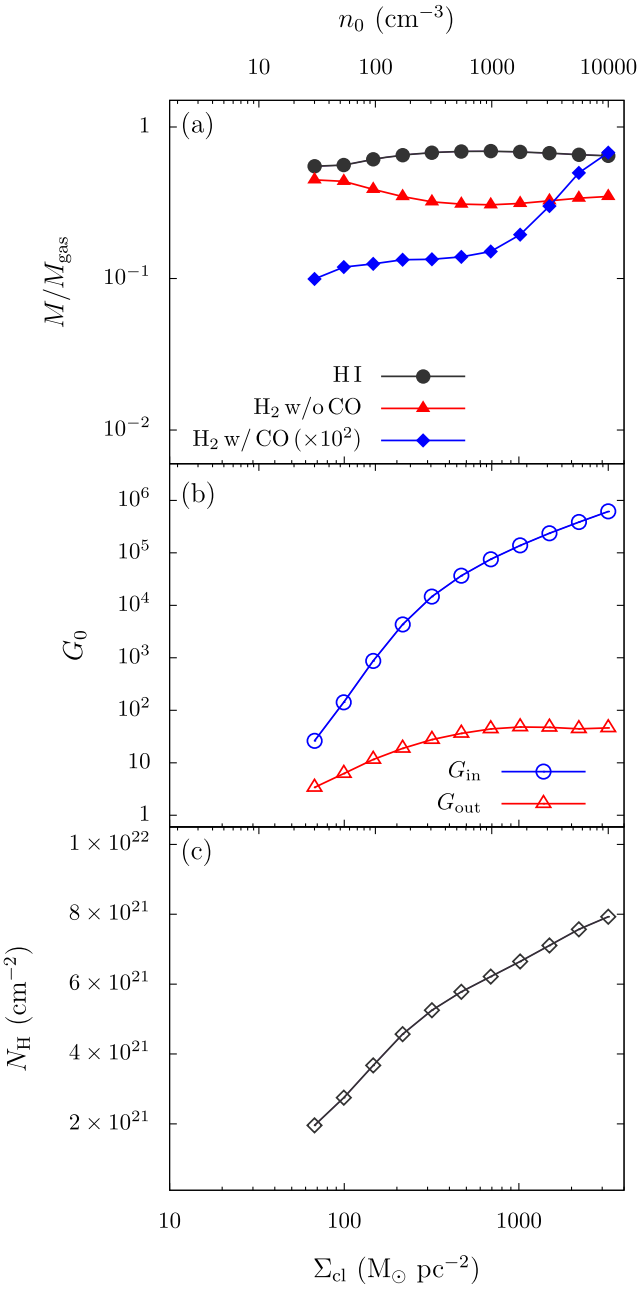

Figure 7. Same as Fig. 6 but for the higher cloud mass of $M_{\rm cl} = 10^6\ {\rm M}_\odot$. In the top panel, the H_2-with-CO fraction for the cases only with the EUV feedback is not presented because it is far below 10^{-5}.

4 DISCUSSION

4.1 Validity of thermal and chemical equilibrium

We have assumed thermal and chemical equilibrium in our modelling, and here we examine the validity of such assumptions. In order to do this, we evaluate the time-scales over which the thermal and chemical equilibrium states, $t_{\rm thm}$ and $t_{\rm chem}$, are achieved. In particular, we consider the H_2 equilibrium time-scale $t_{\rm H_2}$ as $t_{\rm chem}$ because its formation reaction on the grain surface is slowest among the included reactions. We calculate $t_{\rm thm}$ and $t_{\rm H_2}$ using the same method as in Koyama & Inutsuka (2000),

$$t_{\rm thm} = e/\Gamma, \quad (31)$$

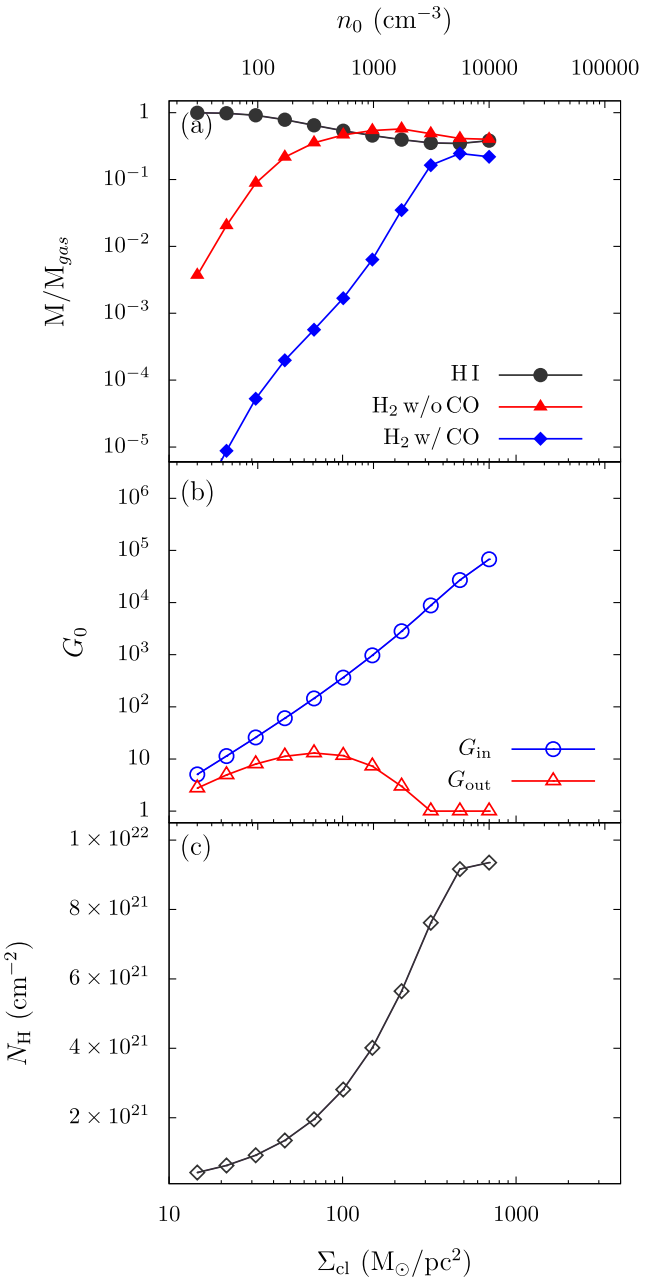

Figure 8. Same as Fig. 6 but for the lower cloud mass of $M_{\rm cl} = 10^4$ M$_\odot$. We do not present the cases only with the EUV feedback unlike Figs 6 and 7, because the resulting minimum SFE is exactly the same (see Section 3.2.1).

$$t_{\rm H_2}^{\rm form} = x_{\rm H_2}/R_{\rm H_2}^{\rm form}, \tag{32}$$

$$t_{\rm H_2}^{\rm diss} = x_{\rm H_2}/R_{\rm H_2}^{\rm diss}. \tag{33}$$

where $R_{\rm H_2}^{\rm form}$ and $R_{\rm H_2}^{\rm diss}$ are the formation and dissociation rates of H_2 molecules, respectively (see equation 13). We use the snapshots at the epochs when the expanding shell reaches the cloud edge at $r = R_{\rm cl}$ (i.e. $t = t_{R_{\rm cl}}$), where the expansion time-scale $t_{R_{\rm cl}}$ corresponds to the dynamical time-scale. The input parameters for calculation are $n = n_0$, $G_0 = G_{\rm out}$ and $N_{\rm H} = N_{\rm H}^{\rm shell}$ (see Figs 9b and c). Inside the shell, in contrast, the average density is

$$\bar{n} = N_{\rm H}^{\rm shell}/dR, \tag{34}$$

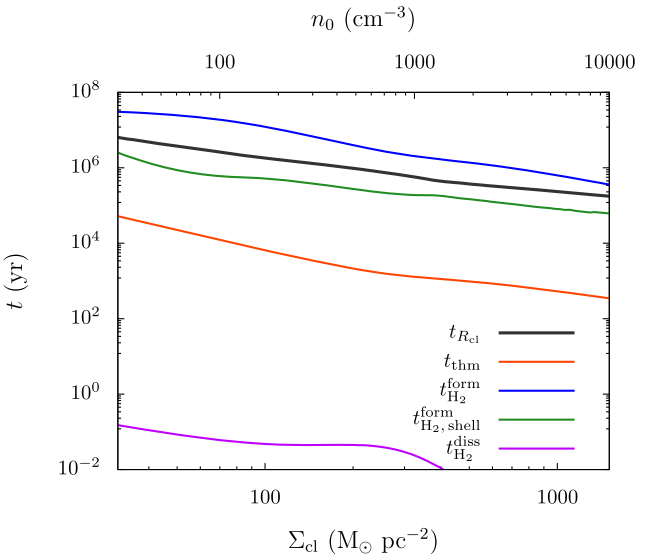

Figure 9. Comparisons of various characteristic time-scales in our calculations with $M_{\rm cl} = 10^5$ M$_\odot$ and different cloud surface density $\Sigma_{\rm cl}$. The snapshots when the minimum SFE is determined with our Criterion 2 are used. Presented are the shell expansion time-scale $t_{R_{\rm cl}}$ (black line), cooling time at the cloud edge (at $r = R_{\rm cl}$, red line), H_2 formation time at the cloud edge (blue line) and on the shell (green line), and H_2 dissociation time at cloud edge (purple line). The average shell density is calculated by equation (34).

where $dR = r_{\rm sh} - r_{\rm IF}$ is the geometrical thickness of the shell, while G_0 and $N_{\rm H}$ are the same as those outside the shell (this treatment is not so accurate, but is a reasonable approximation).

Fig. 9 presents the above time-scales as functions of $\Sigma_{\rm cl}$ for the cases with $M_{\rm cl} = 10^5$ M$_\odot$. We see that all the time-scales gradually decrease with increasing $\Sigma_{\rm cl}$. The dynamical time-scale $t_{R_{\rm cl}} \propto R_{\rm cl}/c_{\rm s,H\,II}$ decreases, because the higher $\Sigma_{\rm cl}$ is, the smaller the cloud size becomes for a fixed cloud mass (equation 1). The chemical and thermal time-scales also drop because collisions, which drive the dominant cooling and chemical processes, occur more efficiently with the higher density. The figure shows that the thermal equilibrium time-scale is always much shorter than the dynamical time, thus supporting our assumption of the thermal equilibrium.

The chemical equilibrium should hold within the dense shell, which carries most of the remnant gas, as the H_2 formation time-scale is comparable to or shorter than the dynamical time $t_{R_{\rm cl}}$ (see the green line). By contrast, the H_2 formation time-scale is longer than $t_{R_{\rm cl}}$ at the cloud edge (see the blue line). This means that the chemical equilibrium of H_2 molecules may not be achieved in the unshocked ambient medium outside the shell by the end of the calculations. However, the clouds we consider are initially fully molecular so that the chemical equilibrium should always be a good assumption even for H_2, because the dissociation time-scale is much shorter than the formation time-scale (see the purple line). Therefore, our conclusion on the chemical composition presented in Section 3.3 will not change much, even if we include the non-equilibrium effects.

4.2 Effects ignored

As already mentioned in Section 2.3.1, our 1D models of the PDR use assumptions for simplicity, such as the optically thin fine-structure line cooling and constant dust temperature throughout a PDR. In order to examine the validity of our treatments, we have also calculated the dynamical evolution of an H II region and surrounding

PDR using a 1D RHD code developed by Hosokawa & Inutsuka (2006) for several representative cases. The RHD code takes into account the effects ignored in the semi-analytical models, such as the trapping effect of the line emission and variable dust temperature. We have confirmed that the simulation results show a similar overall structure of the PDR as provided by the semi-analytical models in spite of numerous differences. For instance, the evolution of the average density within the shell only differs by a few $\times$ 10 per cent between the RHD simulations and the semi-analytical models.

Although our RHD simulations and semi-analytical models employ the same method of Nelson & Langer (1999) for the CO formation rate, there are differences in evaluating the CO photodissociation rate. The semi-analytical models only use the FUV intensity G_i, for which the dust attenuation law is given by the cross-section $\sigma_{\rm d} = 10^{-21}$ cm^2 H^{-1}, to evaluate the CO dissociation rate. The RHD simulations, however, consider another FUV component only representing the CO dissociating band, for which the dust cross-section is larger than the averaged value for the full FUV range $6 \leq h\nu \leq 13.6$ eV. Moreover, the RHD simulations also incorporate the effects of self-shielding and H_2-shielding of CO molecules against dissociating photons (e.g. van Dishoeck & Black 1988). The semi-analytical models thus tend to overestimate the CO photodissociation rate, ignoring these effects. In order to evaluate this effect, we have compared the simulation and model results for the case with $M_{\rm cl} = 10^5$ M$_\odot$ and surface density $\Sigma_{\rm cl} = 300$ M$_\odot$ pc^{-2} (e.g. see Fig. 3 for the model). As shown in Fig. 6, the model predicts that only $\sim$0.1 per cent of the cloud remnant should be H_2 molecular gas associated with CO molecules. The RHD simulation run with the same setting shows that this quantity is $\sim$1 per cent at the epoch when the expanding shell reaches the cloud edge, $t \simeq 6 \times 10^5$ yr since the birth of the H II region. We interpret that such a high value in the simulation run is because the CO dissociation rate is overestimated in the model. If we ignore the effects that are not considered in the model, the simulation returns the lower value $\sim$0.03 per cent. We have also found that the value rapidly rises in the corresponding stage, varying by an order of magnitude in $\sim 10^5$ yr. We conclude that, while there is the general trend that most of the molecular gas contained in the cloud remnants should be CO-dark, the exact amount of CO-bright molecular gas is difficult to estimate accurately. Nonetheless, it would be intriguing to investigate how the dispersing clouds are to be observed as a time sequence. For that purpose, C atoms rather than CO molecules are a more useful tracer of CO-dark gas because of their higher abundance (e.g. Li et al. 2018). Coupling an extended chemistry network beyond the approximation method by Nelson & Langer (1999) with time-dependent hydrodynamics simulations should provide such predictions.

4.3 Other stellar feedback processes

In order to isolate the potential roles of FUV feedback during the cloud disruption, we have employed a simple assumption on the H II bubble expansion (i.e. that the thermal pressure excess of the photoionized gas with respect to the ambient medium drives the expansion). As briefly noted in Section 2.2, theoretical studies suggest that radiation pressure exerted on the shell affects the expansion motion (e.g. Krumholz & Matzner 2009; Fall et al. 2010; Murray et al. 2010; Kim et al. 2016). Such studies all show that the expansion is mainly driven by the radiation pressure rather than the gas pressure if $\Sigma_{\rm cl} \gtrsim 100$ M$_\odot$ pc^{-2}, which is also confirmed by recent numerical simulations, although for turbulent clouds the transition occurs at a higher $\Sigma_{\rm cl}$ (e.g. Kim et al. 2018). Kim et al. (2016) have actually incorporated the effect of radiation pressure in their model by taking $F_{\rm rad} = L/c$ as the average radiation force. We also follow the same approach to modify the temporal evolution of the shell radius given by equation (10). The resulting minimum SFEs for such cases are also presented by the blue dashed line in Fig. 4(b), for which only EUV feedback is assumed (Criterion 1) with $M_{\rm cl} = 10^6$ M$_\odot$. We find that the radiation pressure effect further reduces $\varepsilon_{\rm min}$, and that its effect is more prominent for higher $\Sigma_{\rm cl}$. Inversely, FUV feedback is effective for the low surface density $\Sigma_{\rm cl} \lesssim 100$ M$_\odot$ pc^{-2} (Section 3.2.1), for which the effect of the radiation pressure is limited.

Stellar winds from high-mass stars are also omitted in our models, though they have been referred to as the main driver of the bubble around a massive cluster, including many O-type stars (e.g. McKee, van Buren & Lazareff 1984). The dynamics of the wind-driven bubbles has been modelled assuming spherical symmetry (e.g. Weaver et al. 1977), and it is well described by an expansion law that differs from equation (10). Recent studies further investigate the interplay between the radiation pressure and stellar winds during the bubble expansion (e.g. Rahner et al. 2017, 2019). As we have focused on FUV feedback based on the model of Kim et al. (2016), we have ignored the wind effects following their approach. Regarding the minimum SFEs, we have shown that the FUV feedback is effective for massive GMCs with $M_{\rm cl} \gtrsim 10^5$ M$_\odot$ (Section 3.2). The stellar winds may affect the bubble dynamics for such cases, where the birth of massive clusters with $\gtrsim 10^3$ M$_\odot$ is supposed, assuming $\varepsilon \sim 0.01$. We have also shown that the FUV radiation produces CO-dark gas even for less massive clouds with $M_{\rm cl} \lesssim 10^5$ M$_\odot$ (Section 3.3). The star cluster considered is relatively small with a few O-type stars at most, for which the wind effect should be limited. In any case, recent studies point out that the wind effects on the bubble expansion should be overestimated in 1D modelling. Multidimensional simulations show that the hot gas generated in the wind-driven bubble actually quickly leaks out through low-density channels rather than being confined (e.g. Rogers & Pittard 2013). There are no clear observational signatures that the bubble expansion is evidently driven by the winds (e.g. Lopez et al. 2014). We note that multidimensional effects should also affect the H II bubble dynamics even without wind effects, which is further discussed in Section 4.4.

In this paper, we have considered the stellar feedback on GMCs before the first supernova explosion occurs. As presented in Fig. 9, the dynamical time-scale of an H II bubble expansion is longer for a lower cloud surface density, $\simeq$several $\times$ Myr for $\Sigma_{\rm cl} \lesssim 100$ M$_\odot$ pc^{-2}. This is still shorter than the lifetime of high-mass stars that cause supernova explosions $\sim$10 Myr, but there may not be a long time lag. It is interesting to speculate what happens if a supernova explosion occurs within a cloud under the stellar FUV feedback. Because the supernova explosion adds mechanical feedback on the cloud, it further contributes to reducing the SFE. Moreover, shock waves around the expanding supernova remnant sweep up the gas of the cloud being destroyed, which contains the CO-dark gas under the FUV feedback. As the shock compression is a possible channel of the molecular cloud formation (e.g. Inoue & Inutsuka 2008, 2009), the CO-dark gas may be brought back into the 'CO-bright' molecular phase once the FUV radiation is somehow attenuated. Note that key chemical reactions producing CO molecules near the supernova remnants should differ from those in normal star-forming environments (e.g. Bisbas et al. 2017).

4.4 Inhomogeneous cloud density structure

In our 1D semi-analytical modelling, we have assumed a homogeneous density distribution within a molecular cloud. It is actually possible to relax such an assumption by improving our current model. Kim et al. (2016) have also considered cases with the power-law density distributions $\rho \propto r^{-w}$ with $w < 1.5$. In general,

the photoionized gas expands more rapidly with the less efficient 'trapping' for the cloud with a steeper density gradient (e.g. Franco et al. 1990). An extreme case is known as the 'champagne flow' or 'blister-type' H II regions (e.g. Tenorio-Tagle 1979), for which the gas motion is not adequately described as the pressure-driven expanding shell, but rather as the photoevaporation where the ionized gas freely escapes from the cloud. A fully investigation of the FUV feedback with such a variety of dynamical evolution is out of scope of the current work, but further studies are warranted (e.g. Hosokawa 2007; Geen et al. 2019).

In order to consider the more realistic clumpy cloud structure, one has to resort to three-dimensional RHD numerical simulations. In fact, a number of authors have conducted such simulations, mostly focusing on the stellar EUV feedback (e.g. Walch et al. 2012; see also Section 1). Simulations by Kim et al. (2018) have followed the EUV feedback against clumpy and turbulent GMCs to drive SFEs as functions of the cloud masses and surface densities. They have confirmed qualitative agreements with the model predictions of Kim et al. (2016), but they also found that the model underestimates minimum SFEs compared with the simulation results. The simulations show that the ionized gas escapes from a cloud through low-density parts and the actual feedback is dominated by photoevaporation of surviving clumps. The FUV feedback in the clumpy medium has yet to be fully studied by similar numerical approaches (e.g. Arthur et al. 2011). Although we just have assumed that the star formation is locally quenched in a warm PDR (Section 2.4), it should also be verified with such simulations. Note that the star formation might be rather induced in a clumpy PDR because pre-existing clumps exposed to the FUV radiation would be compressed via the radiation-driven implosion (e.g. Gorti & Hollenbach 2002; Walch et al. 2013, 2015; Nakatani & Yoshida 2019).

5 CONCLUSION

We have developed a semi-analytical model to investigate the FUV feedback on molecular clouds, particularly the effects on the thermal and chemical states of the irradiated gas. On the basis of the previous model by Kim et al. (2016), we have solved the thermal and chemical structure of the PDR as well as the dynamical expansion of an H II region assuming spherical symmetry. We have first evaluated the effects of the FUV feedback on the resulting minimum SFEs supposing that the star formation is suppressed in the warm PDR where the temperature is more than a threshold value (i.e. $\sim$100 K). We have also calculated the chemical composition of the gas that is not converted to stars (i.e. the cloud remnants), under the FUV radiation from the newborn star cluster.

Following Kim et al. (2016), we have calculated the minimum SFEs as functions of the cloud surface density $\Sigma_{\rm cl}$ for different cloud masses of $M_{\rm cl} = 10^4$, 10^5 and 10^6 $M_\odot$. We argue that the FUV feedback is more effective than the pure EUV feedback caused only by the expansion of the H II regions, particularly for massive clouds with $M_{\rm cl} > 10^5$ $M_\odot$ and with the low surface density, $\Sigma_{\rm cl} < 100$ $M_\odot$ pc^{-2}. The minimum SFEs are reduced by the FUV feedback by no less than an order of magnitude when the star formation is assumed to be suppressed above the threshold temperature, 100 K. A key quantity to interpret such dependences is the FUV flux at the cloud edge $r = R_{\rm cl}$ when the cloud is assumed to be disrupted by the EUV feedback, $G_{\rm out}$. If $G_{\rm out}$ is large enough, it means that the cloud is sufficiently heated up by the FUV radiation before the EUV feedback operates, suggesting that the minimum SFE is predominantly determined by the FUV feedback. Our analyses show the scaling relation $G_{\rm out} \propto M_{\rm cl}^{1/2} \Sigma_{\rm cl}^{7/2}$, which explains why the FUV feedback is more effective with a higher $M_{\rm cl}$. The same scaling suggests that $G_{\rm out}$ is smaller with lower $\Sigma_{\rm cl}$ for a given cloud mass $M_{\rm cl}$, which apparently contradicts the trend that the FUV feedback is more effective for the lower $\Sigma_{\rm cl}$. The discrepancy is explained by the fact that the [C II] line cooling, the dominant process, becomes inefficient sharply with decreasing $\Sigma_{\rm cl}$ (or the volume density for a fixed $M_{\rm cl}$). Because of this, the cloud gas tends to be easily heated up even by the weak FUV radiation field. Therefore, the minimum SFE is limited primarily by the FUV feedback with the lower $\Sigma_{\rm cl}$.

Moreover, our analyses on the chemical compositions of the cloud remnants suggest that a large number of them are actually 'CO-dark', except for the cases with $M_{\rm cl} = 10^4$ $M_\odot$ and $\Sigma_{\rm cl} > 300$ $M_\odot$ pc^{-2}. This is because the column densities of the cloud remnants are 2–7 $\times$ 10^{21} cm^{-2} with the wide range of parameters $M_{\rm cl}$ and $\Sigma_{\rm cl}$. With such small column densities corresponding to $A_{\rm V} \simeq$ a few, CO molecules within the cloud remnants are not protected against the incident FUV radiation by the dust attenuation. Only hydrogen molecules survive with the efficient self-shielding effect by contrast. We have also confirmed that such a feature should be the same even for cases where the minimum SFE is primarily limited by the EUV feedback (i.e. where the stellar FUV radiation only plays a minor role in destroying the natal clouds). The dispersed molecular clouds are potential factories of CO-dark gas, which returns into the cycle of the interstellar medium.

ACKNOWLEDGEMENTS

We thank Shu-ichiro Inutsuka for fruitful discussion and comment. This work is financially supported by the Grants-in-Aid for Basic Research by the Ministry of Education, Science and Culture of Japan (16H05996, 19H01934; TH). J.-G.K. acknowledges support from the Lyman Spitzer, Jr. Postdoctoral Fellowship at Princeton University.

DATA AVAILABILITY

The data underlying this article will be shared on reasonable request to the corresponding author.

REFERENCES

Abergel A.Planck Collaboration et al. (Planck Collaboration), 2011, A&A, 536, A21
Arthur S. J., Henney W. J., Mellema G., de Colle F., Vázquez-Semadeni E., 2011, MNRAS, 414, 1747
Bakes E. L. O., Tielens A. G. G. M., 1994, ApJ, 427, 822
Bisbas T. G. et al., 2015, MNRAS, 453, 1324
Bisbas T. G., van Dishoeck E. F., Papadopoulos P. P., Szűcs L., Bialy S., Zhang Z-Y., 2017, ApJ, 839, 90
Butler M. J., Tan J. C., Teyssier R., Rosdahl J., Van Loo S., Nickerson S., 2017, ApJ, 841, 82
Cardelli J. A., Meyer D. M., Jura M., Savage B. D., 1996, ApJ, 467, 334
Cartledge S. I. B., Lauroesch J. T., Meyer D. M., Sofia U. J., 2004, ApJ, 613, 1037
Chabrier G., 2003, PASP, 115, 763
Clark P. C., Glover S. C. O., Klessen R. S., Bonnell I. A., 2012, MNRAS, 424, 2599
Dale J. E., 2015, New Astron. Rev., 68, 1
Dale J. E., Ercolano B., Bonnell I. A., 2012, MNRAS, 424, 377
Diaz-Miller R. I., Franco J., Shore S. N., 1998, ApJ, 501, 192
Draine B. T., 2011, ApJ, 732, 100
Draine B. T., Bertoldi F., 1996, ApJ, 468, 269
Fall S. M., Krumholz M. R., Matzner C. D., 2010, ApJ, 710, L142
Forbes J. C., Krumholz M. R., Goldbaum N. J., Dekel A., 2016, Nature, 535, 523
Franco J., Tenorio-Tagle G., Bodenheimer P., 1990, ApJ, 349, 126
Fukui Y., Kawamura A., 2010, ARA&A, 48, 547

Gaches B. A. L., Offner S. S. R., 2018, ApJ, 854, 156
Gavagnin E., Bleuler A., Rosdahl J., Teyssier R., 2017, MNRAS, 472, 4155
Geen S., Hennebelle P., Tremblin P., Rosdahl J., 2015, MNRAS, 454, 4484
Geen S., Pellegrini E., Bieri R., Klessen R., 2019, MNRAS, 492, 915
Gong M., Ostriker E. C., Kim C-G., 2018, ApJ, 858, 16
González-Samaniego A., Vazquez-Semadeni E., 2020, preprint (arXiv:2003.12711)
Gorti U., Hollenbach D., 2002, ApJ, 573, 215
Grenier I. A., Kaufman Bernadó M. M., Romero G. E., 2005, Ap&SS, 297, 109
Habing H. J., 1968, Bull. Astron. Inst. Netherlands, 19, 421
Haid S., Walch S., Seifried D., Wünsch R., Dinnbier F., Naab T., 2019, MNRAS, 482, 4062
Haworth T. J., Harries T. J., Acreman D. M., Bisbas T. G., 2015, MNRAS, 453, 2277
He C-C., Ricotti M., Geen S., 2019, MNRAS, 489, 1880
Hollenbach D., McKee C. F., 1979, ApJS, 41, 555
Hollenbach D., McKee C. F., 1989, ApJ, 342, 306
Hollenbach D. J., Tielens A. G. G. M., 1999, Rev. Mod. Phys., 71, 173
Hosokawa T., 2007, A&A, 463, 187
Hosokawa T., Inutsuka S-i., 2006, ApJ, 646, 240
Hosokawa T., Inutsuka S-i., 2007, ApJ, 664, 363
Howard C. S., Pudritz R. E., Harris W. E., 2016, MNRAS, 461, 2953
Hu C-Y., Naab T., Glover S. C. O., Walch S., Clark P. C., 2017, MNRAS, 471, 2151
Inoue T., Inutsuka S-i., 2008, ApJ, 687, 303
Inoue T., Inutsuka S-i., 2009, ApJ, 704, 161
Inutsuka S-i., Inoue T., Iwasaki K., Hosokawa T., 2015, A&A, 580, A49
Ishiki S., Okamoto T., 2017, MNRAS, 466, L123
Kennicutt R. C., Evans N. J., 2012, ARA&A, 50, 531
Kim J-G., Kim W-T., Ostriker E. C., 2016, ApJ, 819, 137
Kim J-G., Kim W-T., Ostriker E. C., Skinner M. A., 2017, ApJ, 851, 93
Kim J-G., Kim W-T., Ostriker E. C., 2018, ApJ, 859, 68
Koyama H., Inutsuka S-I., 2000, ApJ, 532, 980
Kruijssen J. M. D. et al., 2019, Nature, 569, 519
Krumholz M. R., Matzner C. D., 2009, ApJ, 703, 1352
Krumholz M. R., Fumagalli M., da Silva R. L., Rendahl T., Parra J., 2015, MNRAS, 452, 1447
Krumholz M. R., McKee C. F., Bland -Hawthorn J., 2019, ARA&A, 57, 227
Langer W., 1976, ApJ, 206, 699
Lee E. J., Miville-Deschênes M.-A., Murray N. W., 2016, ApJ, 833, 229
Li Q., Narayanan D., Davè R., Krumholz M. R., 2018, ApJ, 869, 73
Lopez L. A., Krumholz M. R., Bolatto A. D., Prochaska J. X., Ramirez-Ruiz E., Castro D., 2014, ApJ, 795, 121
McKee C. F., Storey J. W. V., Watson D. M., Green S., 1982, ApJ, 259, 647
McKee C. F., van Buren D., Lazareff B., 1984, ApJ, 278, L115
Matzner C. D., 2002, ApJ, 566, 302
Mellema G., Arthur S. J., Henney W. J., Iliev I. T., Shapiro P. R., 2006, ApJ, 647, 397
Murray N., Quataert E., Thompson T. A., 2010, ApJ, 709, 191
Naab T., Ostriker J. P., 2017, ARA&A, 55, 59
Nakatani R., Yoshida N., 2019, ApJ, 883, 127
Nelson R. P., Langer W. D., 1997, ApJ, 482, 796
Nelson R. P., Langer W. D., 1999, ApJ, 524, 923
Osterbrock D. E., 1989, S&T, 78, 491
Peters T. et al., 2017, MNRAS, 466, 3293
Pineda J. L., Langer W. D., Velusamy T., Goldsmith P. F., 2013, A&A, 554, A103
Pineda J. L., Langer W. D., Goldsmith P. F., 2014, A&A, 570, A121
Rahner D., Pellegrini E. W., Glover S. C. O., Klessen R. S., 2017, MNRAS, 470, 4453
Rahner D., Pellegrini E. W., Glover S. C. O., Klessen R. S., 2019, MNRAS, 483, 2547
Raskutti S., Ostriker E. C., Skinner M. A., 2016, ApJ, 829, 130
Raskutti S., Ostriker E. C., Skinner M. A., 2017, ApJ, 850, 112
Roger R. S., Dewdney P. E., 1992, ApJ, 385, 536
Rogers H., Pittard J. M., 2013, MNRAS, 431, 1337
Seifried D., Haid S., Walch S., Borchert E. M., Bisbas T. G., 2020, MNRAS, 492, 1465
Smith R. J., Glover S. C. O., Klessen R. S., 2014, MNRAS, 445, 2900
Spitzer L., 1978, Physical Processes in the Interstellar Medium. Wiley, New York, .
Tan J. C., Beltrán M. T., Caselli P., Fontani F., Fuente A., Krumholz M. R., McKee C. F., Stolte A., 2014, in Beuther H., Klessen R. S., Dullemond C. P., Henning T., eds, Protostars and Planets VI. Univ. Arizona Press, Tuscon, AZ, p. 149
Tenorio-Tagle G., 1979, A&A, 71, 59
Thompson T. A., Krumholz M. R., 2016, MNRAS, 455, 334
Tielens A. G. G. M., Hollenbach D., 1985, ApJ, 291, 722
van Dishoeck E. F., 1992, in Singh P. D., ed., Proc. IAU Symp. Vol. 150, Astrochemistry of Cosmic Phenomena. Kluwer, Dordrecht, p. 143
van Dishoeck E. F., Black J. H., 1988, ApJ, 334, 771
Walch S. K., Whitworth A. P., Bisbas T., Wünsch R., Hubber D., 2012, MNRAS, 427, 625
Walch S., Whitworth A. P., Bisbas T. G., Wünsch R., Hubber D. A., 2013, MNRAS, 435, 917
Walch S., Whitworth A. P., Bisbas T. G., Hubber D. A., Wünsch R., 2015, MNRAS, 452, 2794
Weaver R., McCray R., Castor J., Shapiro P., Moore R., 1977, ApJ, 218, 377
Whitworth A., 1979, MNRAS, 186, 59
Williams J. P., McKee C. F., 1997, ApJ, 476, 166
Williams R. J. R., Bisbas T. G., Haworth T. J., Mackey J., 2018, MNRAS, 479, 2016
Wolfire M. G., Hollenbach D., McKee C. F., 2010, ApJ, 716, 1191
Wolfire M. G., Hollenbach D., McKee C. F., Tielens A. G. G. M., Bakes E. L. O., 1995, ApJ, 443, 152
Yorke H. W., 1986, ARA&A, 24, 49

APPENDIX: MASS-TO-LUMINOSITY RATIO

To calculate the mass-to-luminosity ratio Ξ for the EUV and FUV radiation from a newborn star cluster, we use the SLUG code, a publicly available spectral population synthesis code (Krumholz et al. 2015). We adopt the same settings as in Kim et al. (2016), i.e. with the IMF given by Chabrier (2003), spectral synthesis model Starburst99, and stellar evolution tracks based on the Genova library. We ran 1000 simulations for each cluster mass bin logarithmically spaced by 0.2 dex in the range of $10^2 \leq M_* \leq 10^5$ $M_\odot$. We assume that the maximum mass of the cluster member star is 100 $M_\odot$. We evaluate the photon number luminosity $S_{\rm EUV}$ and $S_{\rm FUV}$ for the energy ranges of $h\nu > 13.6$ eV (EUV) and $6.0 < h\nu < 13.6$ eV (FUV), respectively.

Fig. A1 presents $\Xi_{\rm EUV}$ (left panel) and $\Xi_{\rm FUV}$ (right panel) as functions of the cluster mass M_*. Each panel shows the 10th to 90th percentile range with the blue shade and the median value with the blue circles connected by the solid line. We see that the EUV ratio $\Xi_{\rm EUV}$ rapidly decreases with a decrease in the cluster mass; the values for 10^3 $M_\odot$ are more than one order of magnitude smaller than those for 10^5 $M_\odot$. By contrast, the FUV ratio $\Xi_{\rm FUV}$ only decreases by a factor of a few, at most, from 10^5 to 10^3 $M_\odot$. This is because, in comparison to the EUV cases, the less-massive stars contribute more to the FUV radiation.

We fit the median value of $\Xi_{\rm EUV}$ and $\Xi_{\rm FUV}$ as the following analytical functions M_*,

$$\log\left(\frac{\Xi_{\rm EUV}}{1{\rm s}^{-1}{\rm M}_\odot^{-1}}\right) = \frac{46.70\chi^6}{2.70+\chi^6}, \tag{A1}$$

$$\log\left(\frac{\Xi_{\rm FUV}}{1{\rm s}^{-1}{\rm M}_\odot^{-1}}\right) = \frac{47.02\chi^6}{0.92+\chi^6}, \tag{A2}$$

where $\chi = \log(M_*/{\rm M}_\odot)$. We have used these formulae in our calculations presented in the main text.

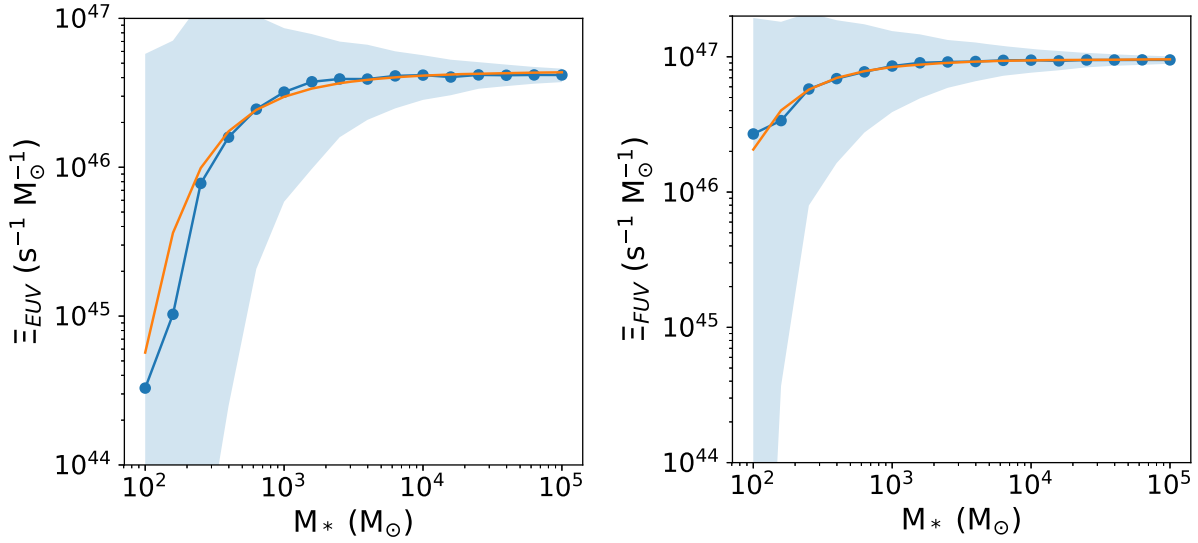

Figure A1. The ratio of EUV and FUV photons emitted per unit time to stellar mass $\Xi_{\rm EUV} = S_{\rm EUV}/M_*$ and $\Xi_{\rm FUV} = S_{\rm FUV}/M_*$. The blue line with circles represents the median values, while the shaded area represents the 10th to 90th percentile range from the simulation. Analytical fitting of the median value is shown with the orange line.

This paper has been typeset from a TEX/LATEX file prepared by the author.